RESEARCH ARTICLE

Key Points:
- Laboratory experiments on shale fault gouge designed to test fault slip behavior during fluid pressurization
- Shale fault gouge fails by accelerated but slow shear slip not evolving into a dynamic slip instability
- Slow shear slip arises from the interplay of fault hydromechanical properties and fault structure evolution

Correspondence to:
M. M. Scuderi,
marco.scuderi@uniroma1.it

Author Contributions:
Conceptualization: Marco M. Scuderi, C. Collettini
Data curation: Marco M. Scuderi
Formal analysis: Marco M. Scuderi
Funding acquisition: Marco M. Scuderi, C. Collettini
Methodology: Marco M. Scuderi, C. Collettini
Writing - original draft: Marco M. Scuderi
Writing – review & editing: Marco M. Scuderi, C. Collettini

Fluid Injection and the Mechanics of Frictional Stability of Shale-Bearing Faults

Marco M. Scuderi[1] and **C. Collettini[1,2]**

[1]Dipartimento di Scienze della Terra, La Sapienza Università di Roma, Rome, Italy, [2]Istituto Nazionale di Geofisica e Vulcanologia (INGV), Rome, Italy

Abstract Fluid overpressure is one of the primary mechanisms for triggering tectonic fault slip and human-induced seismicity. This mechanism is appealing because fluid overpressure reduces the effective normal stress, hence favoring fault reactivation. However, upon fault reactivation models of earthquake nucleation suggest that increased fluid pressure should favor stable sliding rather than dynamic failure. Here we describe laboratory experiments on shale fault gouge, conducted in the double direct shear configuration in a true-triaxial machine. To characterize frictional stability and hydrological properties we performed three types of experiments: (1) stable sliding shear experiments to determine the material failure envelope and permeability, (2) velocity step experiments to determine the rate-and-state frictional properties, and (3) creep experiments to study fault slip evolution with increasing pore fluid pressure. The shale gouge shows low frictional strength, $\mu = 0.28$, and permeability, $k \sim 10^{-19}$ m^2 together with a velocity strengthening behavior indicative of aseismic slip. During fault pressurization, we document that upon failure slip velocity remains slow (i.e., $v \sim 200$ μm/s), not approaching dynamic slip rates. We relate this fault slip behavior to the interplay between the fault weakening induced by fluid pressurization, the strong rate-strengthening behavior of shales, and the evolution of fault zone structure. Our data show that fault rheology and fault stability is controlled by the coupling between fluid pressure and rate-and-state friction parameters.

1. Introduction

During hydraulic fracturing of shale-gas reservoirs, the diffusion of the fluid pressure front can reach ancient faults, modifying the stress field (either directly or indirectly) with the potential for fault reactivation (e.g., Davies et al., 2013; Ellsworth, 2013; Figure 1). One of the primary objectives to mitigate the seismic risk associated to underground fluid injection is to understand what type of slip behavior will be generated upon fault reactivation, whether the fault will fail by earthquake rupture, by accelerated but slow shear slip, or by aseismic creep. A great number of examples have shown that wastewater fluid injection can cause earthquakes with magnitude as large as 5 (e.g., Keranen et al., 2014; Keranen & Weingarten, 2018; Yeck et al., 2017). However, during hydraulic fracturing of shale reservoirs, the moment released by microearthquakes within the stimulated rock volume is much smaller than theoretical prediction based on the amount of fluid injected in the formation, revealing an energy deficit (e.g., Das & Zoback, 2013; Goodfellow et al., 2015; Kumar et al., 2017; Warpinski et al., 2012). Recently, it has been shown that this energy deficit is related with other deformation mechanisms associated with slow but accelerated shear slip along preexisting faults (Boroumand & Eaton, 2012; Caffagni et al., 2016; Das & Zoback, 2013; Eaton et al., 2013; Hu et al., 2017; Kumar et al., 2017; McGarr & Barbour, 2018; Zecevic et al., 2016). In addition, long-period long-duration (LPLD) events are commonly observed during the hydraulic stimulation of shale reservoirs and they have similar characteristics as tectonic tremors observed during slow-slip events at the plate boundary (Kumar et al., 2017). Despite the compelling evidence of slow slip phenomena during fluid pressure stimulations, the physical mechanism at the origin of this slip behavior and the stress conditions required to induce slow-slip are still enigmatic. Furthermore, slow-slip events can act as an efficient mechanism for stress transfer promoting earthquake slip on nearby critically stressed faults (e.g., Elsworth et al., 2016; Guglielmi, Cappa, et al., 2015).

1.1. Fault Reactivation Versus Frictional Stability

The basic physical mechanism to induce fault reactivation is commonly interpreted to follow the effective stress principle (Hubbert & Rubey, 1959):
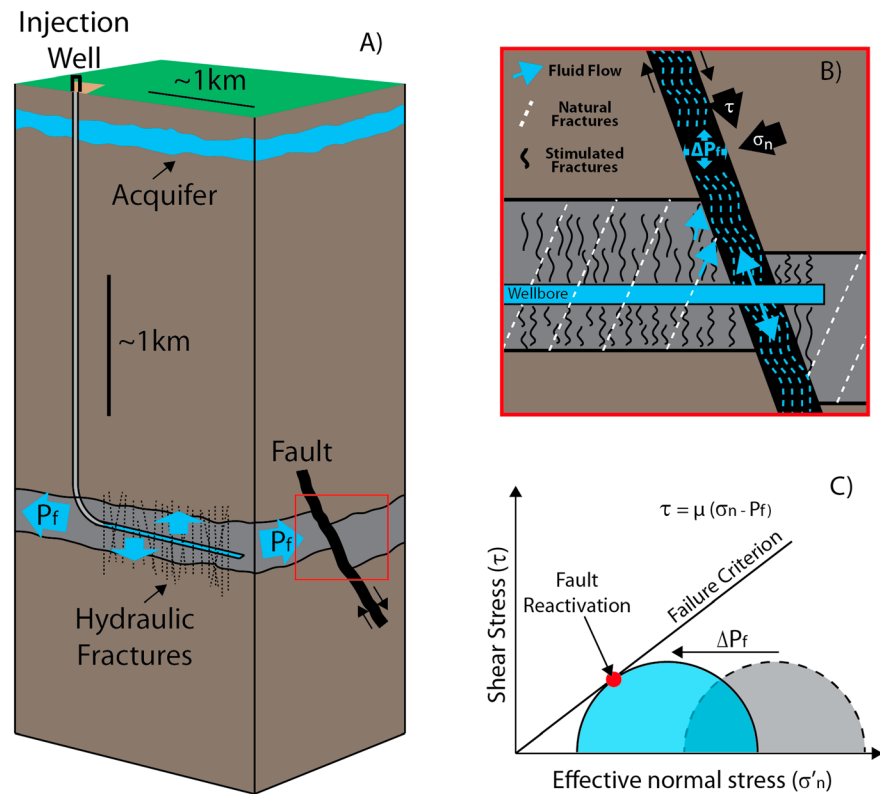
Figure 1. (a) Schematic representation of a typical injection well geometry used during hydraulic fracturing of low permeability gas shales (gray; modified from Davies et al., 2013). The pressurized fluids (blue arrows) can reach ancient critically stressed faults (black). (b) Fluids can infiltrate the fault through different pathways such as natural fractures and/or stimulated fractures reducing the effective normal stress within the fault zone. (c) Schematic representation of a Coulomb-Mohr diagram showing the stress condition along ancient faults before fluid infiltration (gray semicircle). As fluids at high pressure infiltrate within the fault (ΔP_f), the effective normal stress is reduced favoring the conditions for fault reactivation (blue circle).

$$\tau = C + \mu(\sigma_n - P_f) \qquad (1)$$

where τ represents the shear stress at failure, C is the rock cohesion, μ is the fault friction and the difference between the normal stress (σ_n) and the fluid pressure (P_f) represents the effective normal stress (σ'_n; Figure 1b). In this context, an increase in fluid pressure would favor fault reactivation because it decreases the effective normal stress that clamps the fault in place (e.g., Guglielmi, Cappa, et al., 2015; Raleigh et al., 1976). However, equation (1) predicts the stress conditions for fault reactivation but does not give information on the stability of frictional sliding, or in other words whether slip will be seismic or aseismic upon fault reactivation. The rate-and-state friction (RSF) theory is often used to characterize the stability of frictional sliding and evolution of slip behavior by evaluating the velocity dependence of friction (e.g., Aharonov & Scholz, 2018; Dieterich, 1979; Marone, 1998; Ruina, 1983; Scholz, 2002). On the one hand, if the frictional strength decreases as shear slip accelerates the fault has the potential for earthquake nucleation (i.e., velocity weakening, *(a-b) < 0*). On the other hand, faults that are characterized by an increase in frictional strength with increasing shear slip rate are inherently stable (i.e., velocity strengthening, *(a-b) > 0*). Within this framework, for a velocity weakening fault, under constant applied normal stress, the condition for instability to occur is given by the elastic interaction between the surrounding rocks (*k*) and a critical fault rheologic stiffness, defined as (e.g., Gu et al., 1984; Leeman et al., 2016)

$$k_c = \left.(\sigma_n - P_f)(b-a)\middle/ D_c\right. \qquad (2)$$

where *(b-a)* is the friction stability parameter and D_c is the critical slip distance for state evolution. Following this analysis, instability is predicted when the frictional weakening rate of the fault (k_c) is greater than the

energy release rate of the surrounding rocks (k) resulting in force imbalance (i.e., $k < k_c$) and slip acceleration. However, for this system an increase in fluid pressure will tend to favor stable aseismic creep because it decreases k_c (equation (2)), resulting in $k > k_c$. The result of this analysis is that, for a velocity weakening fault, an increase in fluid pressure would favor aseismic creep which is in contrast with observation of induced seismicity. However, Equation (2) was formulated for steady state sliding at constant effective normal stress while during fluid injection the effective stress varies as fluid pressure increases. A modified constitutive law was firstly proposed by Linker and Dieterich (1992) to account for the effect of variations in normal stress on the evolution of the state variable. From linear stability analysis results a critical stiffness of the form (Dieterich & Linker, 1992):

$$k_c = \frac{(\sigma_{n-P_f})(b-a)}{D_c[1 + (\mu - \alpha)tan\ \phi]} \tag{3}$$

where α is an empirical parameter, in the range $0 \leq \alpha \leq \mu$, that couple variation in shear stress associated with changes in normal stress (Linker & Dieterich, 1992), and ϕ is the spring angle, that is, the angle between the fault plane and the maximum principal stress. Stability analysis has shown that for a velocity weakening fault, the stability fields are qualitatively similar to the constant normal stress results derived with equation (2) (Dieterich & Linker, 1992; Gu et al., 1984). The influence of a reduction of normal stress in developing frictional instability has been positively tested on bare surfaces of Westerly granite (Hong & Marone, 2005), but sudden reductions of normal stress on faults consisting of a 50/50 mixture of quartz and smectite, characterized by a velocity strengthening behavior, promoted stable slip. Kilgore et al. (2012), revisited the experiments of Linker and Dieterich (1992) and showed that fault strength does not evolve immediately following normal stress variations suggesting that the unstable response to fault unclamping may be minimized. These contradictory results indicate that additional experimental work is required to assess to role of normal stress perturbations, or a sudden increase in fluid pressure, in the evolution of frictional strength. At the same time it is important to note that at the shallow depth where induced seismicity is observed, 5 to 6 km, and for the fault gouge lithologies involved, frictional sliding is mainly expected in the velocity strengthening regime (e.g., Marone, 1998; Scholz, 1998; Scholz, 2002) as it shown by a great number of experimental work (e.g., Ikari et al., 2009; Kohli & Zoback, 2013; Orellana et al., 2018; Samuelson & Spiers, 2012; Tembe et al., 2010). This observation poses an additional problem in our understanding of the physical mechanisms at the origin of induced seismicity.

1.2. Previous Experimental Work

There is a conspicuous amount of experimental work performed on clay-rich fault gouges because of the important role played by these rocks in unconventional reservoir stability (e.g., Fang et al., 2017; Kohli & Zoback, 2013; Samuelson & Spiers, 2012) and in the hydromechanics of shear zones within the upper crust (e.g., Crawford et al., 2008; Ikari et al., 2009; Tembe et al., 2010; Tesei et al., 2015; Wibberley & Shimamoto, 2003). Many of these works have investigated the effect of clay content by performing experiments on binary mixtures of clay (montmorillonite/illite) and quartz with the characterization of frictional strength, permeability and RSF properties. In general, with increasing clay content it is observed a significant reduction of the coefficient of friction (generally <0.3 for clay content $>50\%$) and a reduction in fault zone permeability, with values as low as 10^{-20} m^2 at high clay content. The RSF parameters are also controlled by the clay content that has the effect of stabilizing shear, inducing a strong velocity strengthening stability regime over a wide range of pressure, temperature, and shear rate boundary conditions (e.g., Den Hartog et al., 2012; Fang et al., 2017; Ikari et al., 2009; Tembe et al., 2010).

Limited laboratory experiments have been specifically designed to investigate the effect of fluid pressure on fault stability (French et al., 2016; Rutter & Hackston, 2017; Sawai et al., 2016; Scuderi et al., 2017). Some of these experiments were performed under triaxial loading conditions with a saw-cut configuration to evaluate the hydromechanical coupling between the rock-matrix and the fault plane. For high porosity and high permeability sandstones, French et al. (2016) find that a reduction in mechanical stress (i.e., lateral expansion achieved by decreasing σ_3) is more efficient in inducing accelerated slip than fluid pressurization. This occurs because a reduction in σ_3 has a more efficient effect on contact-scale stress, producing a more homogenous and rapid stress change, in comparison to fluid pressure buildup, where the associated changes in stress are controlled by fluid diffusion within the fault. Rutter and Hackston (2017) show that the relative permeability

of the rock-matrix compared with hydraulic conductance of the fault controls fault slip behavior. In particular, for a low-permeability rock matrix the generation of hydraulic fractures induced by excess of fluid pressure favors a sudden fluid pressurization along the fault zone causing seismogenic slip in a fault rock that would otherwise slip aseismically. Experiments on blueschist fault gouges at high-pressure and high-temperature show a transition from stable to unstable behavior with decreasing effective normal stress (Sawai et al., 2016). On calcite fault gouges, the weakening induced by fluid pressurization seems to overcome the slightly rate strengthening frictional behavior of the material resulting in fast acceleration and earthquake slip (Scuderi et al., 2017). From the studies mentioned above it arises that fluid pressure plays a strong control on the rheology of fault zone with the potential of inducing slip instability.

The aim of this work is to shed light on the hydromechanical coupling at the origin of fault reactivation and frictional stability during fluid pressure buildup within a shale-bearing fault zone. We developed creep experiments reproducing the boundary conditions of induced seismicity along preexisting ancient faults, where the tectonic shear stress is nearly constant and at critical values (Walsh & Zoback, 2016), and the increase in fluid pressure results in a systematic reduction of the effective stress. We find that increasing fluid pressure causes failure by accelerated but slow shear slip along shale-bearing fault gouge. We couple observations from the evolution of fault slip during fluid pressurization with the fault zone structure and RSF parameters to build a conceptual micromechanical model for the understanding of shale-bearing fault gouge slip behavior during fluid pressure stimulations.

2. Material and Methods

We performed laboratory experiments using a biaxial apparatus (BRAVA, Brittle Rock deformAtion Versatile Apparatus) configured in a double-direct shear (DDS) geometry within a pressure vessel to allow a true-triaxial stress field (Figure 2) (Collettini et al., 2014). In this configuration, a fast-acting horizontal hydraulic servo-controlled ram applies and maintains a constant normal stress (σ_n) on the gouge layers throughout the experiment while a servo-controlled vertical ram is used to apply shear stress (τ) and induce shear deformation within the gouge layers. Applied loads are measured internally to the pressure vessel via strain gauged hollowed load cells (LEANE International model CCDG-0.1-100-SPEC) positioned at the ram nose, with an accuracy of ±0.03 kN over a maximum force of 1.5 MN, that are calibrated regularly. Displacements are measured via linear variable displacement transformers (LVDTs), referenced at the load frame and the moving piston, with an accuracy of ±0.01 μm (Figure 2a). Load point displacement measurements are corrected for the stiffness of the testing apparatus, with nominal values of 386.12 kN/mm for the vertical frame and 329.5 kN/mm for the horizontal frame. Both the horizontal and vertical pistons can be controlled either in displacement control, to advance the ram at constant displacement rate, or load control, to maintain a constant load and measure the resulting displacement. Three hydraulic fast-acting servo-controlled intensifiers were used to apply confining pressure (P_c), upstream and downstream fluid pressure (P_{pu} and P_{pd}, respectively; Figure 2a). Displacements were measured via LVDTs, with an accuracy of ±0.1 μm, and pressures with diaphragm pressure transducers accurate to ±7 kPa. Pore fluid pressure was applied using deionized water to minimize the effects of water chemistry; confining pressure was applied using a hydrogenated paraffinic white oil (vaseline oil viscosity ISO 15). All the output signals were recorded using a simultaneous multichannel analog to digital converter with 24-bit/channel resolution at a sampling rate of 10 kHz, and then averaged for storage at rates between 1 Hz and 10 kHz.

2.1. Sample Preparation and Loading Conditions

We simulated fault gouge using Rochester shale, which is an illite rich shale outcropping in West Virginia (the same rock as in Ikari et al., 2009 and Haines et al., 2013). From X-ray diffraction analysis we retrieved a composition characterized by illite (59%), quartz (23%), kaolinite/dickite (9%), and plagioclase (4%). To produce synthetic fault gouge, intact fragments of Rochester shale were pulverized in a disk mill and hand sieved to a grain size between 63 and 125 μm.

The DDS configuration consists in a three stainless steel block assembly that sandwiches two layers of simulated fault gouge (Figure 2b). The forcing blocks are equipped with conduits to allow fluid flow and connect the gouge layers with the fluid pressure intensifiers (Figure 2b). Sintered porous frits, with a permeability of 10^{-14} m^2, are press fit into cavities within the forcing blocks and used to (1) ensure a homogenous distribution of fluids on the entire sample surface and (2) ensure shear localization within the gouge, and not at the
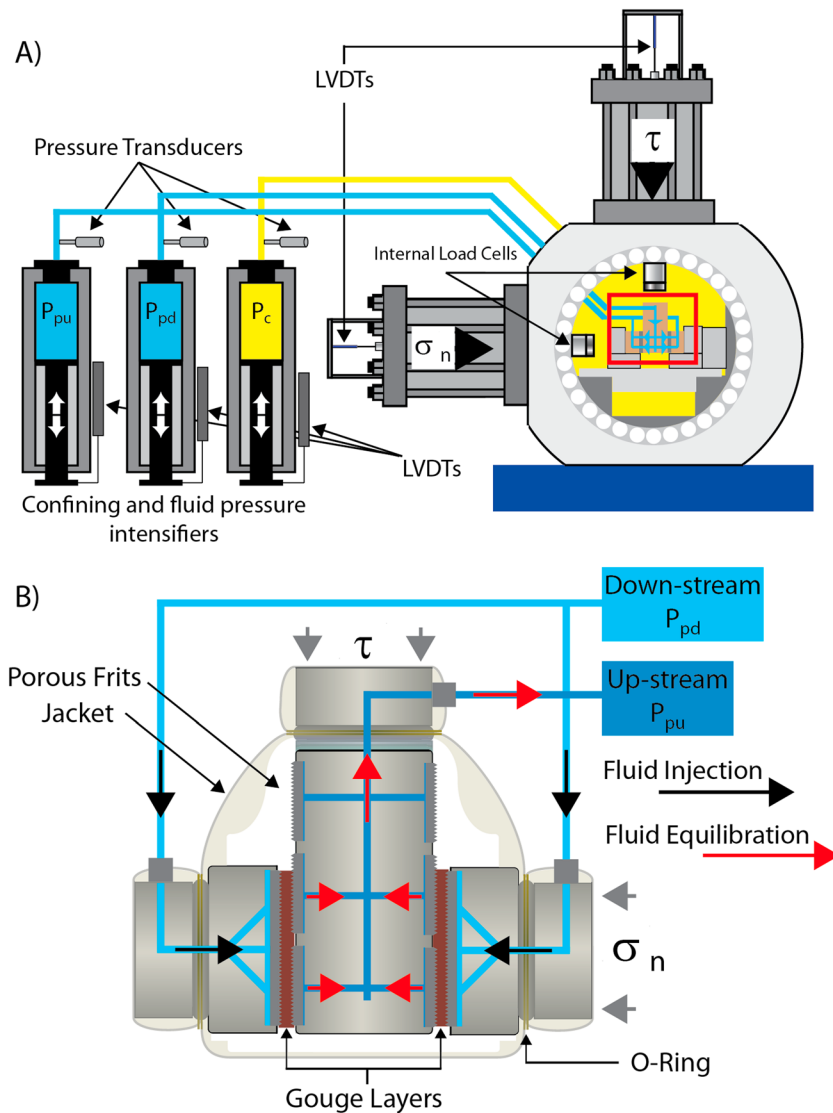
Figure 2. Schematic representation of the experimental configuration. (a) Biaxial rock deformation apparatus configured in a double direct shear configuration within a pressure vessel. Horizontal and vertical rams are used to apply normal (σ_n) and shear (τ) stress, respectively. Three intensifiers are used to apply confining pressure (P_c, yellow), upstream (P_{pu}) and downstream (P_{pd}) fluid pressure. B) Details of the double-direct shear sample assembly (red box in panel (a)). The forcing blocks are equipped with conduits for fluid flow that allow fluid injection from the downstream intensifier (black arrows) and record fluid pressure at equilibrium, after diffusing within the fault gouge, at the upstream intensifier (red arrows).

displacement boundaries, via grooves 0.8 mm in height and spaced 1 mm (Figure 2b). The frits are protected from the gouge powders with filter papers to avoid clogging that would result in a decrease in permeability. For this configuration, the nominal frictional contact area is 5.54 × 5.55 cm and we refer all the measurements of stress, displacement, and pressure changes to one layer.

Gouge layers were prepared using leveling jigs to obtain an initial layer thickness of 5 mm, which was used for all the experiments. During creep experiments, starting porosity can affect time-to-failure and other characteristics of creep behavior (e.g., Baud & Meredith, 1997). For reproducibility of the results, after preparation, the gouge layers were weighed to assure that each experiment started at a similar porosity (Tables 1 and 2). Following this procedure, we obtain variability <6% in initial sample density, which represent the preconsolidation value, that we report as a reference measure to compare initial boundary conditions. However, due to our experimental geometry and loading procedure, we are not capable of accurately measure the compaction during the very initial stage of the experiment. As a result, the density at the onset of shear deformation

Table 1

Summary of Experiments and Boundary Conditions for the Experiments Performed at Constant Displacement Rate to Evaluate Fault Strength (τ_{ss}), RSF Parameters, and Fault Zone Permeability

Exp. number	σ'_n (MPa)	τ_{ss} (MPa)	Starting density (g/cm^3)	Velocity (µm/s)	a	b	D_c (µm)	$(a\text{-}b)$	Permeability (m^2)
b618	10	2.6	1.06	1–3	0.0027	−0.0023	10.22	0.005075	6.97×10^{-19}
				3–10	0.0030	−0.0025	8.34	0.005587	
				10–30	0.0038	−0.0028	9.20	0.006765	
				30–100	0.0046	−0.0051	42.96	0.009827	
				100–300	0.0067	−0.0065	71.81	0.013304	
b617	16	4.5	1.033	1–3	0.0035	−0.0018	32.21	0.005428	1.12×10^{-19}
				3–10	0.0034	−0.0022	21.09	0.00572	
				10–30	0.0033	−0.0034	19.22	0.006852	
				30–100	0.0035	−0.0046	30.39	0.008135	
				100–300	0.0055	−0.0074	65.73	0.0146	
b616	20	5.4	1.094	1–3	0.0035	−0.0017	13.49	0.005323	9.76×10^{-20}
				3–10	0.0029	−0.0028	3.77	0.005771	
				10–30	0.0039	−0.0044	16.74	0.008363	
				30–100	0.0042	−0.0058	33.35	0.010057	
				100–300	0.0060	−0.0081	58.19	0.0158	

Note. The starting density refer to the measure performed on the bench, with no stress applied.

is significantly higher than the value reported in Table 1. We have also conducted two additional experiments at higher preconsolidation sample density (i.e., lower nominal initial porosity) to investigate its effects on creep behavior (Table 2). Once the gouge layers were prepared, the sample assembly (i.e., gouge layers + forcing blocks) was jacketed to separate the gouge layers and pore fluid from the confining oil (Figure 2b and details in Scuderi & Collettini, 2016).

Each experiment followed a common starting loading procedure, for reproducibility and comparison purposes. For our sample geometry and dimension, the confining pressure contributes to the total normal stress resulting in the effective normal stress (σ'_n) acting on the gouge layers given by: $\sigma'_n = (\sigma_n + P_c) - P_f$. We started by applying the confining pressure at steps of 1 MPa every 3 min until the target value was reached and it was maintained constant throughout the experiment. Subsequently, the horizontal ram was advanced at constant displacement rate until contact with the sample was established and a small force was applied. At this point we switched the control feedback to load-mode and reached the target value that was maintained constant throughout the experiment. With this configuration, we are capable of resolving fine details of the

Table 2

Summary of Experiments Performed under Creep Conditions

Exp number	$\tau\%$	Injection protocol	Starting density (g/cm^3)	μ_{peak}	μ_{ss}	γ onset creep	h onset creep (mm)
b621	90	1 MPa/h	1.056	0.3	0.27	17.5	0.75
b656	90	0.2 MPa/12 min	1.043	0.3	0.27	16.8	0.76
b664	90	Constant	1.017	0.31	0.27	18.3	0.598
b736	80	1 MPa/h	1.069	0.3	0.27	17.3	0.798
b620	80	1 MPa/h	1.258	0.31	0.28	9.8	1.357
b630	80	0.2 MPa/12 min	1.237	0.3	0.26	13.3	0.937
b733	80	0.2 MPa/12 min	1.029	0.29	0.27	17.4	0.65
b734	80	Constant	1.024	0.32	0.28	22.1	0.522

Note. All the experiments started at an effective normal stress $\sigma'_n = 20$ MPa given by $\sigma_n = 5$, $P_c = 28$, and $P_f = 13$ MPa. We report the values of friction at peak (μ_{peak}) and steady state (μ_{ss}). We also report the values of shear strain (γ onset creep), layer thickness (h) at the onset of the creep test and starting density measured on the bench, with no stress applied.
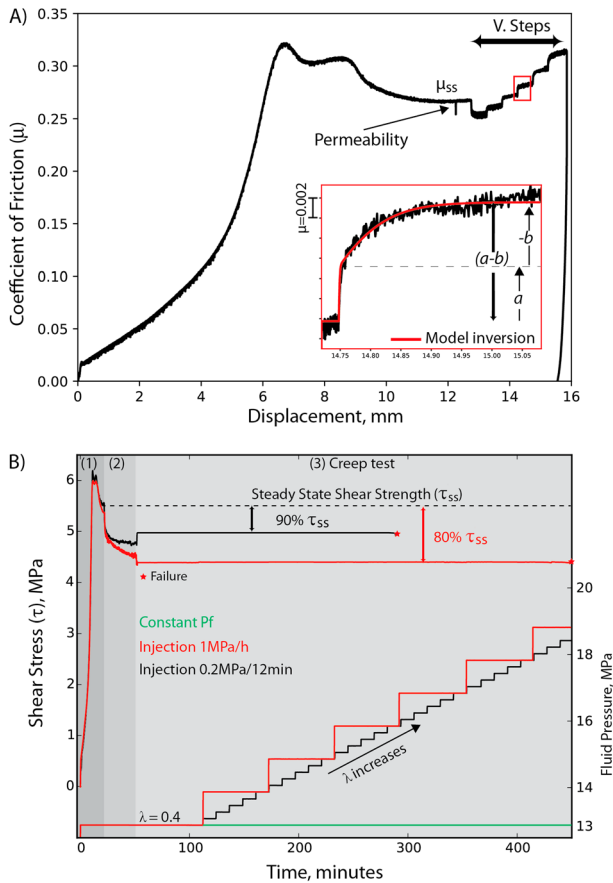
Figure 3. Experimental procedure. (a) Typical experimental curve, showing the evolution of frictional strength with accumulated displacement (exp. number b617). Shear is first imposed at 10 μm/s until a steady state frictional sliding regime is achieved (μ_{ss}). Permeability is measured at steady state shear under quasi static conditions. Afterwards velocity steps are imposed to evaluate rate-and-state friction parameters. Inset shows a velocity step (black curve) with the result of the model inversion (red curve) used to determine rate-and-state friction parameters. (b) Typical experimental curves for two experiments (exp. number b656 and b733) showing the evolution of shear stress with time. (1) Shear is imposed at a constant displacement rate, and then it is stopped and the fault relaxes in (2). (3) During the creep test, a constant shear stress at either 80% (red curve) or 90% (black curve) relative to the steady state strength (τ_{ss}) is imposed, and fluid pressure is increased at either 1 MPa/hr (red curve) or 0.2 MPa/12 min (black curve). For reference, we performed experiments at constant fluid pressure (green curve).

evolution of gouge layer thickness (h) that in our experiments can be considered as a proxy for porosity changes, after correcting for the geometrical layer thinning due to our DDS geometry (e.g., Scott et al., 1994). Once the layer thickness achieved stable values under these stress conditions (usually 30–40 min), we started to apply the pore fluid pressure by advancing the upstream intensifier until a small pressure, usually 1 MPa, was achieved, while the downstream intensifier was left open to the atmosphere until flow through was established. At this stage, the gouge layers are fully saturated, we closed the downstream intensifier to the atmosphere and waited (usually 2 hr) for equilibration with the upstream pressure. Pore fluid pressure was then increased at steps of 1 MPa every 30 min until the target value was reached, and the sample was left to equilibrate overnight while creep compaction occurred and the gouge layers achieved a steady state thickness. At this point shear began, and we followed two different experimental protocols: (1) constant displacement rate experiments to evaluate fault strength and fault permeability and characterize the RSF properties and (2) creep experiments to evaluate the evolution of slip behavior as a function of fluid pressurization. All experiments started under hydrostatic fluid pressure condition as expressed by the pore fluid factor, $\lambda = P_f/\sigma_n = 0.4$, and under nominally drained boundary conditions.

2.2. Fault Strength, Permeability, and RSF Properties

We conducted experiments at values of effective normal stress (σ'_n) of 10, 16, and 20 MPa under hydrostatic (i.e., $\lambda = 0.4$) and nominally drained boundary conditions. Shear stress was applied by advancing the vertical ram at constant displacement rate of 10 μm/s until a residual steady state strength (μ_{ss}) was achieved (Figure 3a). To reach steady values of μ_{ss} we usually shear for ~12 mm of displacement, that correspond to shear strain >10, which is indicative that shear fabric fully developed within the gouge layers (Figure 3a; e.g., Haines et al., 2013). At this point we stopped the vertical ram and measured fault zone permeability, under quasi-static stress conditions, by applying the constant head method (e.g., Ikari et al., 2009). This method consists in applying a differential pressure between P_{pu} and P_{pd} (usually 1 MPa) and measure the resulting flow rate. Permeability was then calculated using Darcy's law:

$$k = \frac{Q\eta}{A}\frac{dl}{dP_p} \tag{4}$$

where k is the sample permeability (m^2), A is the frictional contact area (m^2), η is the viscosity of the water (1.002×10^{-9} [MPa*s]), dP_p is the imposed differential pressure (MPa), and dl is the sample layer thickness (m), measured as the initial layer thickness and changes recorded by the horizontal LVDT. Q represents the average flow rate (m^3/s) across the layers as measured at the upstream ($dP_{pu-disp}/dt$) and downstream ($dP_{pb-disp}/dt$) intensifiers. To ensure accurate measurements of permeability, since the permeability of the gouge is low, we waited to flow through the gouge layers at least 5026.54 mm^3 of water (which correspond to ~1 mm of intensifiers displacement, given a radius of 40 mm), which is comparable to the sample volume at the onset of the measurements. Following this procedure, we ensure steady flow conditions, with a flow rate difference between $Q_{upstream}$ and $Q_{downstream}$ less than 5%.

At the end of the permeability test, we resumed shear at 10 μm/s and performed a series of velocity steps, with shear velocities ranging between 1 to 300 μm/s, to evaluate the velocity dependence of friction and infer the stability of frictional sliding (Figure 3a). To investigate fault slip stability and retrieve the RSF

parameters we modeled each velocity step following the general formulation of the rate-and-state friction constitutive equation (Dieterich, 1979; Marone, 1998; Ruina, 1983):

$$\mu = \mu_0 + a \ln\left(\frac{v}{v_0}\right) + b \ln\left(\frac{\theta v_0}{D_c}\right) \qquad (5)$$

where μ_0 represent a reference coefficient of friction at sliding velocity v_0, v is the frictional slip rate, and a and b are empirical constants (e.g., Ikari et al., 2016). D_c is the critical slip distance, which is interpreted as the distance required to renew a population of asperity contacts, and θ is the state variable, representing the average contacts lifetime. We coupled equation (5) with a description of the state evolution, that here we choose as the law proposed by Ruina (1983):

$$\frac{d\theta}{dt} = -\frac{v\theta}{D_c} \ln\left(\frac{v\theta}{D_c}\right) \qquad (6)$$

The choice of this evolution law is motivated by recent observation showing a better fit to experimental data (e.g., Bhattacharya et al., 2017; Kaneko et al., 2016). To take in account for the finite stiffness of our experimental apparatus and its elastic interaction with the gouge layers, we couple equations (5) and (6) with the time derivative of a simple spring equation:

$$\frac{d\mu}{dt} = k\left(v_{lp} - v\right) \qquad (7)$$

where v_{lp} is the load point velocity and k is the stiffness (given in units of μm^{-1}) measured from the loading slope of velocity steps (Blanpied et al., 1998; Reinen & Weeks, 1993; Saffer & Marone, 2003). Because k can slightly vary as a function of confining pressure, we determined a single value of k, usually in the range $0.005 < k < 0.008 \ \mu m^{-1}$, for each experiment and used it for all the inversions concerning those data. To obtain rate-and-state parameters a, b, and D_c, we solve equations (5) and (6) using a fifth-order Runge-Kutta numerical integration technique with adaptive step-size, with equation (7) as a constraint. The best-fit values of the constitutive parameters are determined using an iterative, least-square method. For a typical model fit the unweighted chi square error is usually ≤ 0.0001, and the variance is $\leq 5 \times 10^{-7}$. The estimated error is calculated from the covariance matrix and expressed as one standard deviation, which is usually ≤ 0.0002. These errors are usually smaller than the uncertainties associated with experimental reproducibility.

2.3. Creep Experiments

Each creep experiment began at a value of effective normal stress of 20 MPa, under hydrostatic boundary conditions (i.e., $\lambda = 0.4$) and is characterized by a common, three stage, experimental procedure (Figure 3b). First, shear stress was applied at a constant displacement rate of 10 $\mu m/s$ until a steady state sliding regime (τ_{ss}) was achieved, usually after 12 mm of displacement, corresponding to shear strain >10, to form a shear fabric within the gouge layers (Table 2). Second, the vertical ram was stopped and we let the sample relax for 30 min until a residual shear strength was achieved. This stage was necessary to ensure crack closure and the best packing configuration. Third, we started the creep test by switching the vertical ram control from displacement- to load-mode feedback control and set the shear stress at either 80% or 90% relative to the steady state shear strength (Figure 3b and Table 2). Under these conditions, we maintain a constant shear stress, with an estimated variation of ± 2 kPa around the target value, and measure the resulting true fault slip. The sample was left to creep for 1 h under hydrostatic conditions to ensure the achievement of a steady creep before injection began. Fluid pressure was increased stepwise from the downstream intensifier and recorded at the upstream intensifier after that the fluid pressure front diffused within the gouge layers, with fluid circulation and equilibration modulated by the permeability of the fault gouge. We followed two different injection protocols: (1) we increased fluid pressure at 1 MPa/hr or (2) we increased P_f at 0.2 MPa/12 min. For comparison purposes, we have performed experiments where the fault gouge was left to creep under hydrostatic boundary conditions and at constant fluid pressure (Figure 3b).
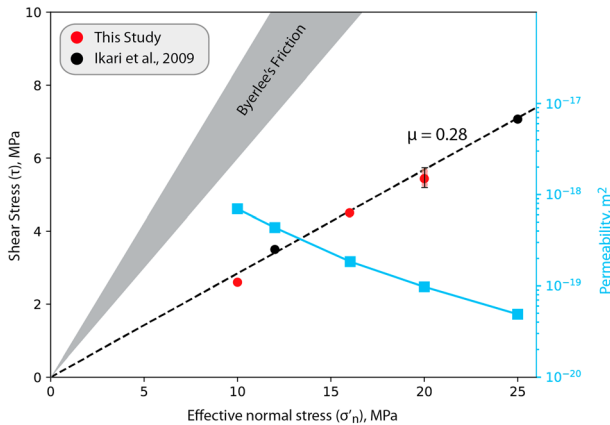
Figure 4. Coulomb-Mohr failure diagram reporting the values of shear strength measured at different effective stresses together with the values measured by Ikari et al., 2009. The linear failure envelope results in a coefficient of friction of $\mu = 0.28$ that is low compared with Byerlee's friction (i.e., 0.6–0.8; gray area). Permeability is reported as a function of effective normal stress (blue points).

3. Results

3.1. Frictional Strength and Permeability

We measured the frictional strength of the fault gouge at values of σ'_n of 10, 16, and 20 MPa, and under hydrostatic boundary conditions ($\lambda = 0.4$; Figure 3a). The experimental curves show a peak strength followed by a strain weakening stage and the attainment of a residual steady state strength (μ_{ss}), for values of shear strain >10. The values of steady state shear stress (τ_{ss}) scale linearly with increasing effective normal stress and can be fitted accordingly to the Coulomb-Mohr criterion (equation (1)) yielding a value of $\mu = 0.28$ that is in agreement with previously reported data for the same material (Figure 4; Ikari et al., 2009). To note the high reproducibility of the experiments as shown for the nine experiments conducted at $\sigma'_n = 20$ MPa that show a variability <6% (Figure 4 and Tables 1 and 2).

Fault zone permeability was measured after the fault gouge attained a residual steady state strength (μ_{ss}), to ensure a meaningful measure after shear deformation localizes. As expected, permeability decreases as the effective normal stress is increased ranging from $k = 6.97 \times 10^{-19}$ m^2 at $\sigma'_n = 10$ MPa, to $k = 9.76 \times 10^{-20}$ m^2 at $\sigma'_n = 20$ MPa (Figure 4). These very low values of permeability are expected for clay-rich fault gouge and compare very well with the measurements performed by Ikari et al. (2009) for the same fault gouge material or previous studies on clay-rich fault gouge (Brown et al., 2003; Crawford et al., 2008; Morrow et al., 2017; Wibberley & Shimamoto, 2003).

3.2. Frictional Constitutive Properties

We measured the velocity dependence of friction to retrieve fault constitutive parameters by performing velocity step sequences at $10 < \sigma'_n < 20$ MPa, under hydrostatic boundary conditions (Figure 5 and Table 1). The fault gouge shows a clear velocity strengthening behavior (i.e., $(a-b) > 0$) for all the range of boundary conditions of stress and shear velocity tested in this study (Figure 5a). The friction rate parameter $(a-b)$ does not show any clear dependence on the applied effective normal stress but it has a positive dependence on shear velocity, with values that range from ~0.005 to ~0.015 as slip rate is increased (Table 1). We find that $(a-b)$ is roughly constant for shear velocity ≤ 10 μm/s, showing a gradual increase as the shear rate is increased (Figure 5a). The friction rate parameter a is always greater than b, which is at the origin of the velocity strengthening behavior; both a and b depend on sliding velocity and are independent of the applied effective normal stress (Figure 5b). We find that a shows constant values until a shear velocity of 10 μm/s, afterwards it increases as shear velocity is increased. The friction rate parameter b is always characterized by negative values, and it is roughly constant for shear velocity ≤ 10 μm/s, followed by a decrease as shear rate is increased. A negative value of the rate parameter b is commonly observed for phyllosilicate rich fault gouges under fluid-saturated conditions (Fang et al., 2017; Faulkner et al., 2018; Ikari et al., 2009; Kohli & Zoback, 2013; Tembe et al., 2010). The critical slip distance, D_c, exhibits a similar dependency on slip velocity as described above and we do not find any dependence with σ'_n. D_c is generally small for velocities ≤ 30 μm/s, with values ranging between $3 < D_c < 30$ μm, and gradually increases as shear rate is increased reaching final values of 50–70 μm that are almost doubled when compared to the initial values (Figure 5c).

3.3. Slip Behavior During Fault Gouge Creep

To evaluate slip stability during fluid pressurization we developed creep experiments where the shear stress is maintained constant, at either 90% or 80% relative to the steady state shear strength (τ_{ss}), and fault slip is monitored during fluid pressurization (Figures 6 and 7 and Table 2). Each creep test began at similar values of shear strain to ensure that the starting microstructures (i.e., initial shear fabric and porosity) were similar between experiments. Figure 6 shows typical curves of slip and slip velocity for the experiments performed at 90% of τ_{ss} along with the corresponding evolution of the stress state represented in a Coulomb-Mohr diagram. In general, the curves do not show the typical trimodal creep behavior commonly observed for creep experiments on intact rocks (e.g., Brantut et al., 2013) or granular fault gouge (e.g., Scuderi et al., 2017). The trimodal slip behavior usually consists in a primary or decelerating creep, followed by a secondary or steady
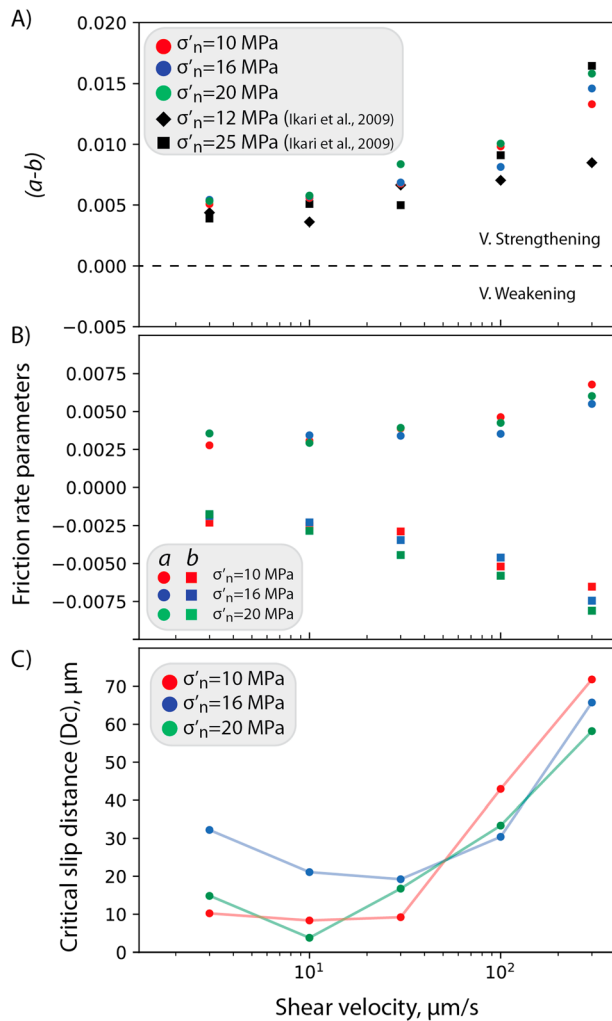
Figure 5. Evolution of the rate-and-state friction parameters obtained after model inversion. (a) Evolution of the stability parameter *(a-b)* as a function of the imposed slip velocity for all the effective normal stresses investigated. For comparison, we report the data of Ikari et al., 2009 at comparable effective normal stresses. (b) Evolution of the friction rate parameter *a* (circles) and *b* (squares) as a function of slip velocity for different effective normal stresses. (c) Evolution of the critical slip distance (D_c) as a function of slip velocity for different effective normal stresses.

creep until the critical conditions for slip acceleration are reached and the tertiary creep begins until dynamic slip propagates. Here, at the beginning of each creep stage, we do not observe any primary or decelerating creep, but fault slip increases monotonically in time at slip velocities of ~20 nm/s, accumulating ~70 μm of displacement (Figures 6a and 6b). The absence of primary creep can be due to compaction creep, likely accommodated via crack closure and porosity reduction, during the hold stage performed before the onset of creep (Figure 3b). At the beginning of fluid pressurization, we observe a marked acceleration of fault slip with a net deviation from the experiment performed at constant fluid pressure (Figure 6b). During fluid pressurization we observe that the fluid injection procedure controls the time to failure and slip behavior. For the experiment where fluid pressure was increased at steps of 1 MPa/hr we observe that slip abruptly accelerates corresponding to the fluid pressure step followed by a deceleration and sliding at a new constant higher velocity (Figure 6b). Near the stress state for fault reactivation (yellow portion of the diagrams in Figure 6) the fault gouge, upon the step of P_f, first accelerates, then it decelerates before evolving into a final slow acceleration (Figure 6). To note that this final acceleration does not show the typical shear velocity of dynamic slip associated with tertiary creep (e.g., Moore & Iverson, 2002; Rathbun et al., 2008; Heap et al., 2009; Brantut et al., 2013; Scuderi et al., 2017), that rapidly evolves to slip velocity >mm/s. Here the slip velocity remains slow, with a peak of ~200 μm/s, for the accumulated displacement of ~11 mm over a duration of ~25 min. For the experiment where fluid pressure was increased at 0.2 MPa/12 min, as fluid pressurization begins, we observe a continuous exponential increase in fault slip (i.e., log-linear relation with time; Figure 6a). The slip velocity increases over four orders of magnitude during fluid pressurization as we approach the stress state for reactivation (Figure 6b). The onset of accelerated failure (red portion of the diagrams in Figure 6), is marked by a slow acceleration that reaches a peak velocity of ~200 μm/s over ~11 mm of displacement and a duration of ~17 min. For this injection protocol, as we approach the stress state for reactivation, small acceleration and deceleration correspond to each fluid pressure step (Figure 6b). In addition, we observe that the stress state required for accelerated failure is 600 kPa greater than that predicted by the Coulomb-Mohr failure envelope, which is at the origin of the longer time to failure when compared with the experiment where P_f was increased at 1 MPa/hr.

The experiments conducted at 80% of τ_{ss} show similar features of fault slip evolution as for the suite of experiments performed at 90% of τ_{ss} (Figure 7). At the onset of creep, before fluid pressurization begins, fault gouge creeps at velocity of ~1 nm/s, without showing the primary creep stage. For this stress field, as pressurization begins, the fault gouge continues to creep at constant slip rate and deviates from the experiment at constant fluid pressure after P_f was increased of 2 MPa and the stress state was closer to the Coulomb-Mohr criterion for failure (green portions of the diagrams in Figure 7). At this point, as observed for the experiments at 90% of τ_{ss}, the injection protocol of 1 MPa/hr causes an abrupt acceleration corresponding with each fluid pressure step, followed by a deceleration and sliding at a new higher velocity (Figures 7a and 7b). As we approach the critical stress state for reactivation, the fault gouge slowly accelerates reaching a peak velocity of ~100 μm/s for an accumulated displacement of ~11 mm over a duration of 21 min. When fluid pressure was increased at 0.2 MPa/12 min fault gouge slip evolution is characterized by an exponential increase of slip and slip velocity for fluid pressure in the range $14.4 < P_f < 16$ MPa, accumulating ~500 μm of slip. For fluid
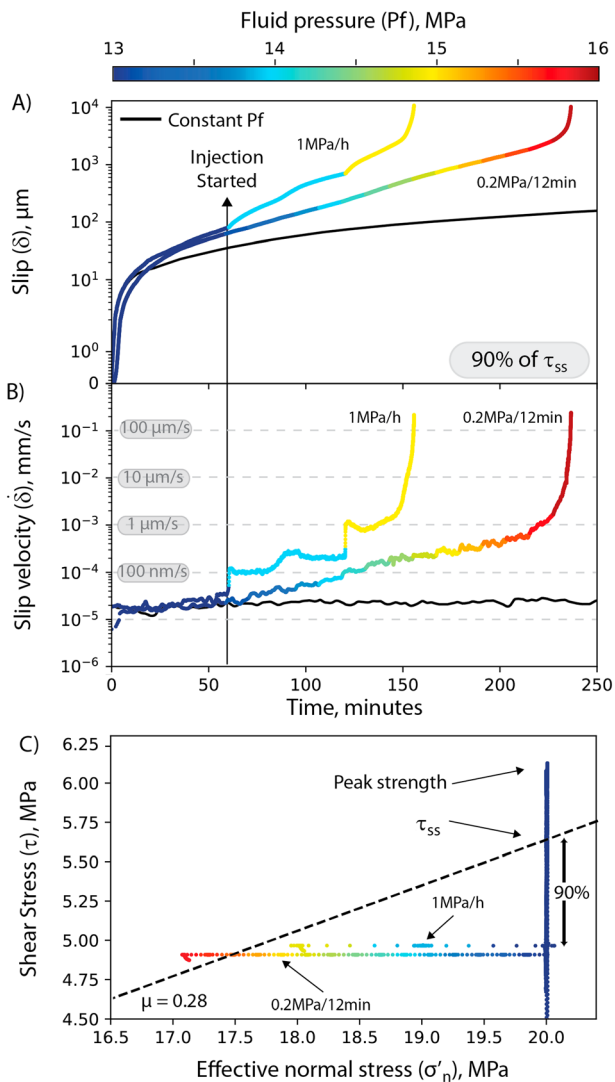
Figure 6. Raw data showing the time series of the evolution of fault slip (a) and slip velocity (b) for the experiments performed at 90% of τ_{ss}. The curves are color coded by the applied fluid pressure at the downstream intensifier (injection side). In black is reported the experiment performed at constant fluid pressure. (c) Coulomb-Mohr failure diagram showing the evolution of the stress state during injection. Dashed line represents the failure envelope obtained from friction tests (Figure 4). Note that the stress path during creep at 1 MPa/hr has been slightly offset to avoid overlap.

pressure > 16 MPa we observe that small fault accelerations and decelerations are modulated by steps in fluid pressure and remain below a velocity of 1 μm/s. At the critical stress state for reactivation fault gouge slowly accelerates, reaching peak slip velocity of ~100 μm/s, for an accumulated slip of ~11 mm, over a time of 17 min.

To summarize our observations, increasing fluid pressure induces fault gouge acceleration well before reaching the Coulomb-Mohr criterion for reactivation. Steps in fluid pressure cause fault accelerations that are followed by decelerations, modulated by the magnitude of the fluid pressure step. At the critical stress state for reactivation, during failure, fault slip velocity remains slow even for large (>10 mm) accumulated displacement.

3.4. Evolution of Layer Thickness and Volumetric Strain

During each experiment, we track variations in volumetric strain during gouge deformation to gain insights into the micromechanical behavior of the fault during slip (Figure 8). We monitor the changes in layer thickness (Δh) that represent a direct proxy for volume changes since the nominal friction contact area remains constant throughout the experiment (e.g., Samuelson et al., 2009). At the onset of the creep stage, when fluid pressure was kept constant at $\lambda = 0.4$, we always observe fault zone compaction for all the range of stress conditions explored (Figures 8 and 9b) while slip velocity remains constant (Figures 6 and 7). This is consistent with the experiments performed at constant fluid pressure showing compaction creep throughout the creep stage. In the experiments where fluid pressure was increased, the onset of fluid pressurization causes fault gouge to dilate (Figure 8). In general, we observe that dilation persists during the first stages of fluid pressurization while the fault is sliding at very slow slip rate and the stress state is far from reactivation. The absolute value of dilation is variable between experiments and does not correlate with applied shear stress but it is slightly modulated by the injection procedure. Commonly, the gouge layers dilate 0.17% to 0.37% compared to the initial layer thickness. As fluid pressure is further increased and we approach the critical stress state for reactivation we observe an abrupt change from dilation to compaction while slip velocity is increasing. However, this abrupt change in volumetric deformation does not correlate with the evolution to tertiary creep as previously observed in similar creep experiments on calcite fault gouge (Scuderi et al., 2017). Although interesting, more experiments are needed to fully understand the micromechanical processes governing this transition. Compaction persists until the final stages of fault acceleration, where, before reaching the maximum displacement attainable in our experiments, we always observe fault zone dilation (Figure 9b). However, due to the finite amount of displacement of our experimental geometry, it is not possible to understand if during this stage further dilation would cause fault to decelerate (e.g., Segall & Rice, 1995).

3.5. Effect of Initial Porosity on Fault Slip Behavior

Minor variations in fault gouge porosity can strongly influence frictional and hydrologic properties as well as slip behavior during creep experiments, because they can control the degree of shear localization and consequently fluid diffusivity across the fault gouge (e.g., Baud & Meredith, 1997; Anthony & Marone, 2005). In Figure 9 we compare experiments performed at the same boundary conditions of stress and injection procedure, but starting with different sample density of $\Delta\rho = 0.208$ g/cm^3, resulting in different porosity (Table 2). In the following, we will show only the case of 80% of τ_{ss} and injection of 0.2 MPa/12 min; however, the same relations are found for the 1 MPa/hr injection case (Table 2).
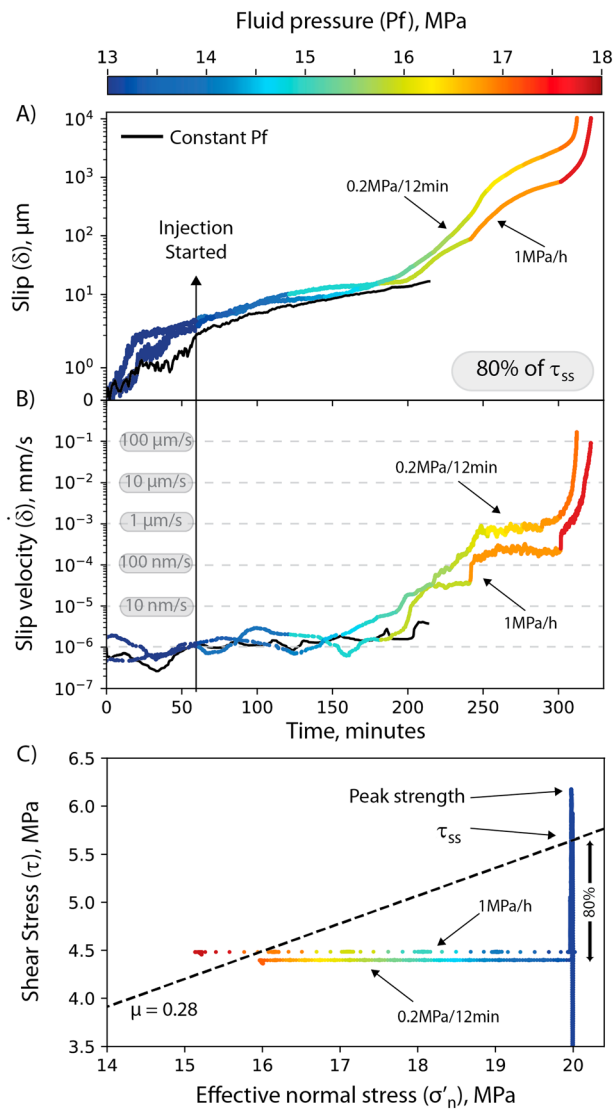
Figure 7. Raw data showing the time series of the evolution of fault slip (a) and slip velocity (b) for the experiments performed at 80% of τ_{ss}. The curves are color coded by the applied fluid pressure at the downstream intensifier (injection side). In black is reported the experiment performed at constant fluid pressure. (c) Coulomb-Mohr failure diagram showing the evolution of the stress state during injection. Dashed line represents the failure envelope obtained from friction tests (Figure 4). Note that the stress path during creep at 1 MPa/hr has been slightly offset to avoid overlap.

Our data show that initial density influences the time to failure, with the experiment performed at greater density ($\rho_1 > \rho_2$) showing a longer time to failure resulting in a greater fluid pressure, of 2 MPa, required to induce failure and accelerated slip (Figure 9a). However, the evolution of slip behavior is comparable between the two experiments. In both cases, initial creep velocity is in the order of 1 nm/s, with accelerated creep starting as we pressurize the fault, moving the stress state toward reactivation. Strikingly, in both cases, we observe a threshold in slip velocity of ~1 µm/s where small accelerations and decelerations, modulated by steps in fluid pressure, propagate. Finally, as we reach the critical stress state for reactivation the fault gouge fails by accelerated creep with peak slip velocity that remains slow, in the order of ~200 µm/s, for an accumulated displacement of ~11 mm, over a duration of ~20 min. The evolution of gouge layer thickness shows that at the onset of fault creep, when fluid pressure is still constant, in both cases, fault zone compacts and slips at constant velocity (Figure 9b). As we increase fluid pressure, fault zone undergoes dilation, with the gouge at greater density (ρ_1) showing greater dilation when compared to the gouge at lower initial density (ρ_2). At the critical slip velocity of ~1 µm/s, in both cases, we observe a sharp change from dilation to compaction that persists during the small accelerations and decelerations modulated by fluid pressure steps. During the last stage of acceleration, at velocity ~10 µm/s, layer thickness reaches a plateau followed by fault dilation, which is more evident for the experiment at greater initial density. Our data show that starting porosity influences time to failure and the stress state for reactivation, but it does not change the main characteristics of slip behavior in response to fluid pressurization.

3.6. Hydrological Behavior

Diffusion of the fluid pressure within the fault gouge can influence the mode of fault slip depending on the capability of the gouge layers to efficiently drain and diffuse fluid pressure, a property that is controlled by fault permeability (e.g., Fang et al., 2017; Faulkner et al., 2018; Ikari et al., 2009; Morrow et al., 2017; Samuelson et al., 2009; Segall & Rice, 1995; Wibberley & Shimamoto, 2003). During our experiments the fluid pressure is increased from the downstream intensifier and fluid pressure equilibration is recorded at the upstream intensifier after diffusion through the gouge layers (Figure 2b). In Figure 10 we show the fluid pressure equilibration curves for two typical creep experiments performed at 80% of τ_{ss} and injection of 1 MPa/hr (Figure 10a) and 0.2 MPa/12 min (Figure 10b). For injection at 1 MPa/hr we find that in response to an instantaneous increase in fluid pressure (black curve), the fluid pressure front slowly diffuses within the fault gouge with equilibration time varying from 28 to 33 min, having the classical shape of a diffusio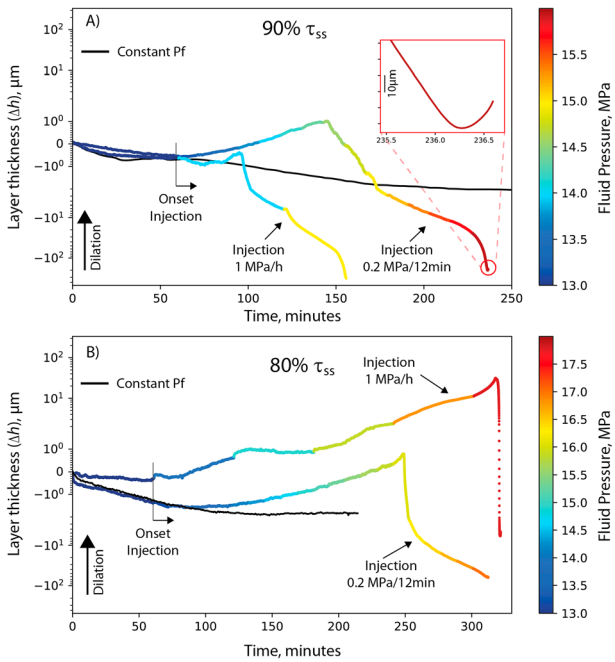n profile for low permeability fault gouge (e.g., Faulkner et al., 2018; Shapiro et al., 2002). Following the analysis of Ikari et al. (2009) (their equation (10)) we can write the permeability as a function of diffusion time:

$$k = \frac{h^2 \beta_p \eta}{2t} \tag{8}$$

where k is the permeability (m²), η is the water viscosity (8.9×10^{-4} [Pa*s]), β_p is the compressibility of the gouge layers that we assume in the range of plastic to medium hard clay ($1.0845e^{-6}$ [m²/N]; Domenico & Mifflin, 1965), h is the layer thickness that we continuously monitor (Table 2), and t is the diffusion time that we retrieve from our experiments. The values of permeability that we obtain from this analysis are in the range of 9.3×10^{-20} to 1.1×10^{-19} m² which are in good agreement with the measured values, via

Figure 8. Time series showing the evolution of layer thickness (dilation positive) for the experiments performed at (a) 90% and (b) 80% of τ_{ss}. For each panel are reported the two injection experiments (i.e., 1 MPa/hr and 0.2 MPa/12 min) color coded by the injection pressure at the downstream intensifier (injection side), and in black the experiment performed at constant fluid pressure.

equation (2), at the steady state frictional sliding, that are in the range 9.7×10^{-20} at $\sigma'_n = 20$ MPa and 6.9×10^{-19} at $\sigma'_n = 10$ MPa (Figure 4 and Table 1). From the analysis of the equilibration time, for the creep tests during fault pressurization we do not find any measurable change of fault zone permeability, which does not show any systematic evolution either with accumulated fault slip or layer dilation/compaction. We note that variations in permeability and fluid diffusivity would be very small, given the very low permeability of the fault gouge and therefore we think that cannot be captured in our analysis. Furthermore, we measure permeability perpendicular to the shear direction and not along the parallel direction which should represent the preferential path for permeability enhancement (e.g., Faulkner & Rutter, 2001; Kawano et al., 2011). When the fluid injection was 0.2 MPa/12 min we find that in response to a pressure step from the downstream intensifier, fluid pressure diffuses, however, the noise in the data, due to the very small pressure step and low permeability, does not allow a correct evaluation of the diffusion time. Nonetheless, we note that the upstream fluid pressure (equilibration) follows the downstream (injection), implying that fluid pressure diffuses within the gouge and is at equilibrium after each pressure step (Figure 10b).

3.7. Microstructural Observations

At the end of selected experiments, we collected the resulting fault gouge for microstructural analysis at the scanning electron microscope (Figure 11). Shear is accommodated by cataclasis and grain size reduction in the bulk volume of the fault gouge, where fractured and rounded quartz grains and aggregates of illite are randomly oriented (Figure 11a). Deformation is localized along both incipient R_1-planes, which start from the boundaries of the gouge layers, and sharp and continuous B-planes (e.g., Logan et al., 1979). The incipient R_1-planes form at low angle with the direction of shear and are characterized by a thickness of ~10–20 μm (Figure 11b). Within the R_1-planes we document grain size reduction and an S-C mechanical foliation. We observe B-shear planes on both sides of the fault zone. Their thickness varies between ~150 μm on the injection side to ~50 μm on the stationary side and are characterized by an intense grain size reduction when compared to the bulk volume of the fault gouge (Figure 11a). Within the B-shear planes, part of the deformation is accommodated by frictional sliding along the clay minerals that are oriented in the direction of shear, forming discrete Y-shear planes (Figure 11c). The Y-planes bound lenses of more competent material (i.e., quartz) showing different degree of fracturing and resulting in variable grain dimensions (in the order of 30–40 μm; Figures 11b–11e). Shear along the illite layers is often observed (red arrows in Figure 11c), and it is usually interpreted to be at the origin of frictional weakness (i.e., μ = 0.28).

4. Discussion

4.1. The Mechanics of Clay Fault Gouge During Fluid Pressurization

In this study, we have designed experiments to evaluate the evolution of clay-rich fault slip behavior under conditions of fluid pressurization, which find direct application to natural and induced seismicity (e.g., Davies et al., 2013). By developing creep experiments, where the shear stress is maintained constant and at critical values (i.e., either 80% or 90% of τ_{ss}), we aim at capturing the hydromechanical coupling that controls fault slip along clay-rich fault zones during fluid injection stimulations. Our data show that at the critical stress state for reactivation, failure is characterized by slow but accelerated shear slip, with slip velocity that remains below 200 μm/s even for large displacements (>10 mm) and long durations (>20 min), not approaching the typical values for dynamic slip instability (i.e., velocity > mm/s). Slow shear slip upon fault failure is independent of applied shear stress and injection procedure indicating that, under the conditions explored in our study, this is a universal failure mechanism within shale-bearing fault gouge.

In the following we will focus on second order variations in fault slip behavior before failure to couple hydrologic and mechanical behavior with the fault zone structure and propose a conceptual micromechanical

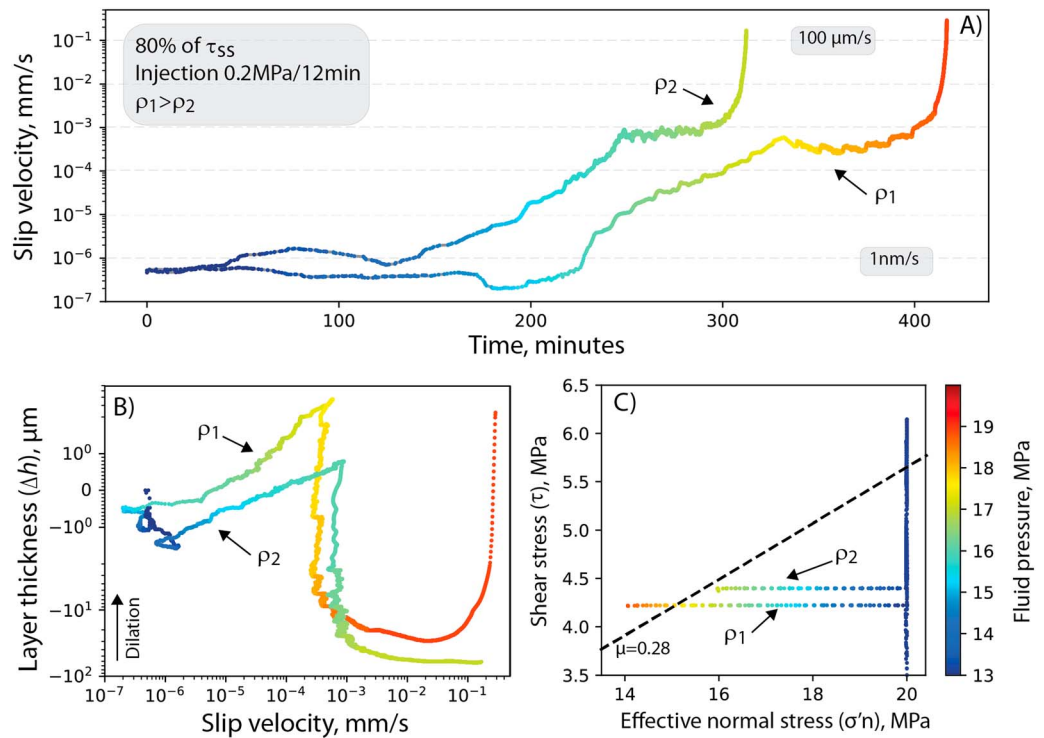**Figure 9.** Comparison of experiments performed at different initial density and same stress (80% of τ_{ss}) and injection procedure (0.2 MPa/12 min; exp. number b630 and b733). All the curves are color coded by the injection fluid pressure at the downstream side (injection). (a) Time series of the evolution of slip velocity during pressurization. (b) Relation between the evolution of layer thickness (dilation positive) and slip velocity during fluid pressurization. (c) Coulomb-Mohr diagram showing the evolution of the stress field during fluid injection. Black dashed line represents the failure envelope obtained from friction tests (Figure 4).

model to shed light on the physical processes governing slow shear slip under fluid injection conditions. The fluid injection procedure is the main parameter that controls second order fault gouge variations in slip behavior before failure, indicating that fluid diffusion processes are coupled with fault deformation resulting in the observed fault slip behavior. For injection at 1 MPa/hr we always observe that slip velocity
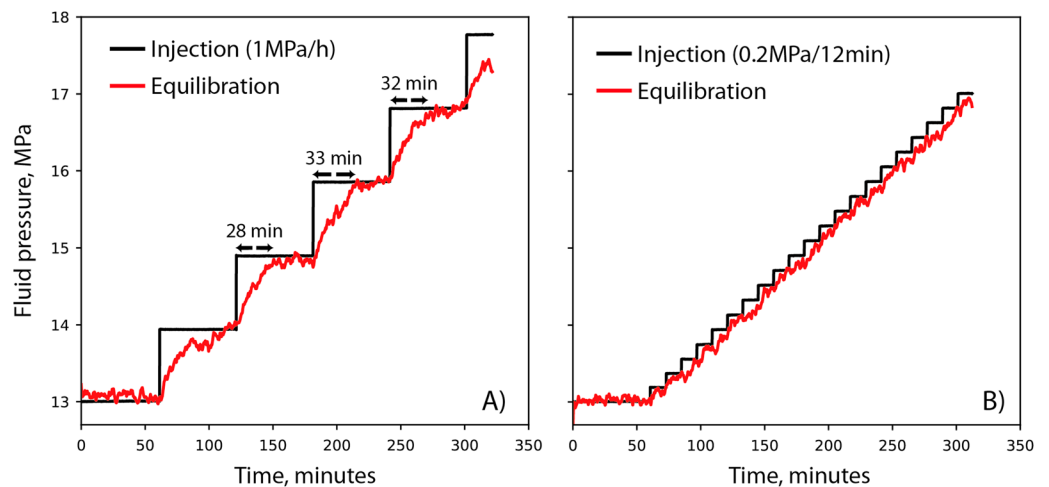

Figure 10. Fluid injection curves for two experiments performed at 80% of τ_{ss} and injection protocol of (a) 1 MPa/hr and (b) 0.2 MPa/12 min (exp. number b736 and b733 respectively). In black is reported the fluid pressure at the injection side (downstream intensifier) and in red fluid pressure equilibration (upstream intensifier) following fluid pressure diffusion within the gouge layers.
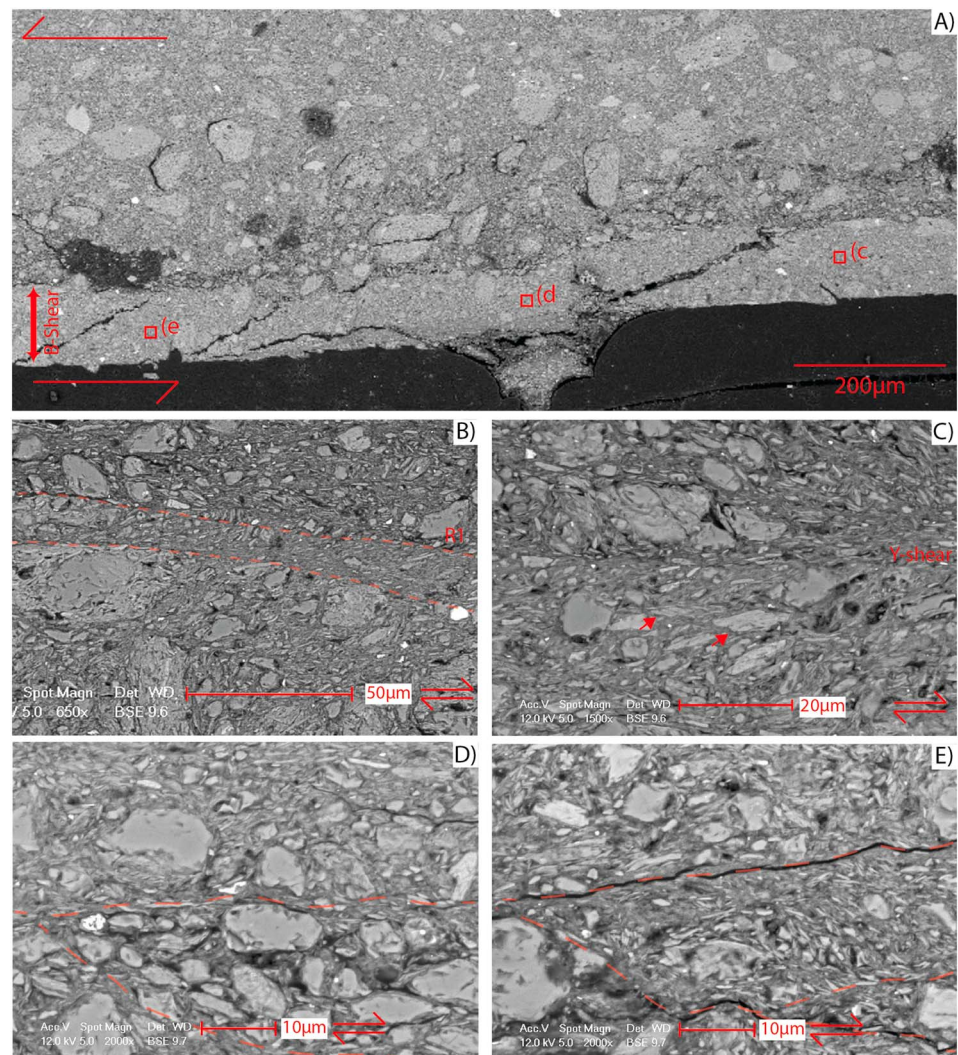
Figure 11. Fault zone microstructure after shear of a typical experiment performed at 80% of τ_{ss} (exp. number b733). (a) Shear localizes along continuous B-shear planes showing strong grain size reduction when compared with the bulk volume of the gouge layer. (b) Incipient R1 shear planes develop from the boundaries of the sample and are characterized by a mechanical S-C foliation. ((c)–(e)) Details of the shear fabric within the B-shear zone. Illite minerals are aligned in the direction of shear forming Y-shear planes that bound lenses of fractured quartz grains. Shear within illite-rich surfaces is often observed (red arrows in (a)).

increases upon a fluid pressure step, evolving to a new steady state velocity after some evolution time (Figures 6 and 7). For this injection procedure, the fault approaches a new steady velocity after that all the fluid pressure diffused within the fault gouge and equilibrated at the upstream intensifier reaching homogenous stress conditions (Figure 10). The jump in slip velocity is usually ~1 order of magnitude, up to the final slow acceleration, characterized by an increase over ~2 orders of magnitude, from 1 to ~200 μm/s, over a duration >20 min. For the 80% of τ_{ss} case, each pressure step causes accelerated slip and fault gouge dilation that is an efficient mechanism to dissipate fluid overpressure. At 90% of τ_{ss}, dilation is not as persistent as for 80% of τ_{ss} (Figure 8a vs. b).

For the injection protocol of 0.2 MPa/12 min we observe that once fluid pressurization begins and the stress state is far from the reactivation criterion (13 < P_f < 14.4 MPa for 90% of τ_{ss} and 14.4 < P_f < 15.6 MPa for 80% of τ_{ss}), fault slip velocity increases following an exponential trend with accumulated slip (i.e., log-linear relation in Figures 6b and 7b), while the fault is dilating (Figure 8). During this stage, while the fault is accelerating the accumulated shear strain is very small ($\gamma < 1$, taken from the beginning of the creep test, Figure 12) suggesting that deformation is distributed within the bulk volume of the fault gouge. Near the critical stress state
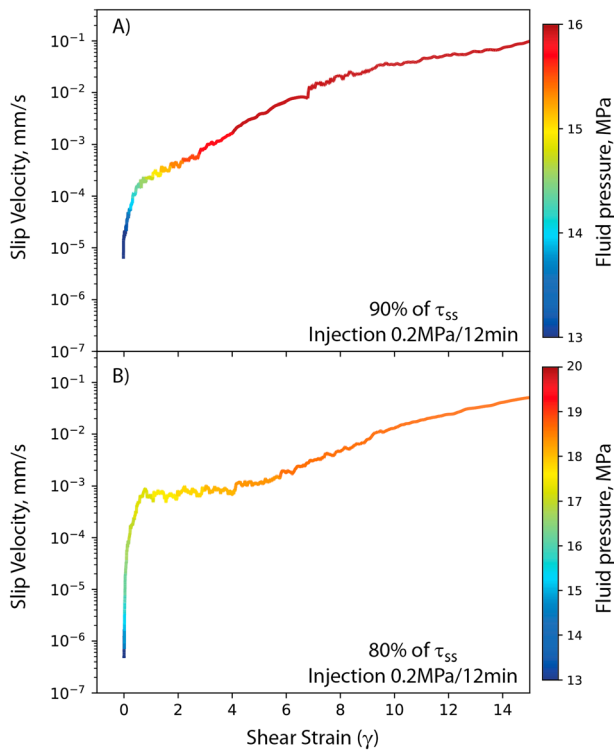
Figure 12. Evolution of slip velocity as a function of shear strain, calculated from the beginning of the creep test, for two typical experiments performed at 90% (a) and 80% (b) of τ_{ss} and injection protocol of 0.2 MPa/12 min (exp number b656 and b733). All the curves are color coded by the fluid pressure at the injection side (downstream intensifier).

for reactivation small accelerations and slow decelerations begin and are induced by the step in fluid pressure (Figure 9a). Common for both the applied shear stresses (i.e., 80% or 90% of τ_{ss}) the onset of small accelerations and slow decelerations coincides with an evolution from gouge dilation to compaction attained at slip velocity $\leq 1~\mu m/s$ (Figures 8 and 9b). We posit that the sharp evolution from fault gouge dilation to compaction (Figure 8), coupled with significant shear strain accumulation (Figure 12), is the indication of shear slip along illite rich slip zones (Figure 11; Den Hartog & Spiers, 2014; Niemeijer & Spiers, 2007). In these experiments the evolution of fluid pressure does not show any short-term trend due to the noise in the data associated with the very small pressure steps. However, we note that at the end of each 0.2 MPa step, the upstream pressure is always equilibrated, indicating that fluid pressure diffused within the gouge layers (Figure 10).

In light of these observations, for a fault gouge near the critical stress state for reactivation, we propose a deformation mechanism that couples fault gouge mechanical and hydrological properties during fluid pressurization (Figure 13). In response to a fluid pressure step, the localized and clay-rich Y-shear planes, within the B-shear zone, form barriers for fluid flow, due to the very low permeability, and can undergo local fluid overpressure inducing semidrained fluid flow conditions (Stage 1 in Figure 13; e.g., Faulkner et al., 2018; Wibberley & Shimamoto, 2003). This local fluid overpressure can significantly decrease the effective stress along the localized Y-planes, inducing accelerated slip (Figure 13b, inset). With ongoing slip, the anastomosed fabric of the Y-shear planes allows fluid overpressure diffusion, also facilitated by the preferential fluid pathways created by the fractured quartz grains (Stage 2 in Figure 13). As the fluid pressure diffuses within the bulk volume of the fault gouge, and local fluid overpressure is reduced, fault slip decelerates (Figure 13b, inset). In this context, we do not expect to observe the same effect of fluid pressurization on slip behavior within the B-plane at the opposite side of the fault zone because fluids diffuse slowly toward it, preventing the generation of fluid overpressures. When all the fluid pressure is equilibrated and the new stress state is homogenous within the fault, the fault slips at constant velocity that is higher compared to the velocity at the previous stress state. In this context, we posit that slip is accommodated along the Y-shear planes where the illite sheets are aligned in the direction of shear and are intrinsically velocity strengthening resisting slip acceleration. The result is that slip velocity during the pressurization stages and the final acceleration remain slow because of the strongly velocity strengthening properties of the clay-rich fault gouge (Stage 3 in Figure 13, see discussion below).

4.2. RSF Friction Behavior Versus Accelerated Creep

Our rate-and-state friction analysis shows that for a range of effective normal stresses the fault gouge shows a marked velocity strengthening behavior, with the stability parameter *(a-b)* that increases as slip velocity is increased (Figure 5). The analysis of the friction rate parameters shows two fundamental characteristics: (1) a negative value of the rate parameter *b*, which would greatly favor fault stable creep, since friction evolves to a higher value with increasing velocity and (2) an increase in the critical slip distance, D_c, above a shear velocity of 30 $\mu m/s$ which should also favor stable aseismic creep. The coupling of these observations would imply that our clay-rich fault gouge is not a candidate for seismic nucleation. However, in our creep experiments, during fluid pressurization we document accelerated fault creep, that contrasts with the inferred stability regime derived from RSF parameters measured during velocity steps experiments showing velocity strengthening behavior. Our RSF data are in very good agreement with previous work performed on the same fault gouge (e.g., Ikari et al., 2009) and with other studies that investigated frictional stability on synthetic mixtures and natural samples of quartz/illite (Saffer & Marone, 2003; Brown et al., 2003; Tembe et al., 2010; Samuelson & Spiers, 2012; Kohli & Zoback, 2013; Wojatschke et al., 2016; Fang et al., 2017; Orellana et al., 2018). In most of these studies, a strong velocity strengthening behavior was observed, and when
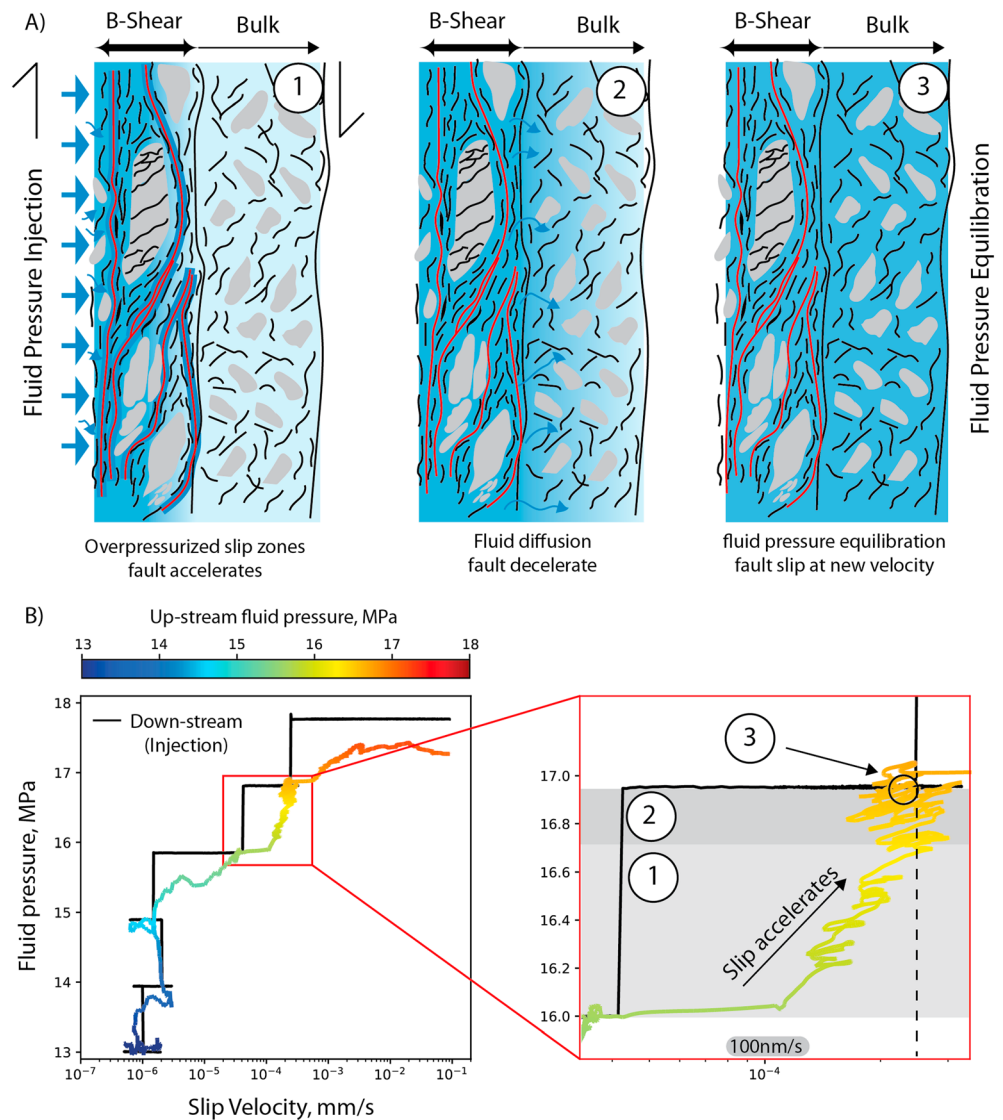
Figure 13. (a) Conceptual micromechanical model describing the evolution of fault zone deformation for shale-bearing fault gouge under fluid pressurization conditions. (b) Relation between fluid pressure and slip velocity for the experiment b733. In black is reported the fluid pressure at injection and the fluid pressure at equilibrium is color coded by the pressure recorded at the upstream intensifier (equilibration; e.g., Figure 10). The inset represents a typical fluid pressure step where all the three stages of the proposed model can be individuated, see text for details.

the fault gouge was saturated with fluids, a negative value of the rate parameter *b* is documented (Fang et al., 2017; Ikari et al., 2009; Tembe et al., 2010). The physical mechanism at the origin of negative *b* is still elusive, however, Ikari et al. (2009) proposed that a combined effect of clay frictional properties and poroelastic stress changes, associated with fault dilation and local fluid depressurization, can act in concert during velocity step sequences and result in a marked velocity strengthening behavior. Faulkner et al. (2018) proposed that above a threshold shear velocity (0.03 μm/s) fluid overpressure may develop, associated to fault compaction, within clay gouge layers due to the low permeability (i.e., semidrained condition). They propose that the effect of fluid pressure development can alter the RSF analysis leading to misleading interpretations, with velocity weakening occurring in a velocity strengthening material as a result of fluid overpressure. Our observations during creep experiments coupled with the proposed micromechanical model (Figure 13) show that the slip behavior of shale fault gouge is controlled by transient weakening induced by fluid pressure that results in fault slip acceleration. Then, upon fluid diffusion and equilibration, the fault slips at a new steady state velocity that remains slow given the intrinsic velocity strengthening properties. Similar

slip behavior is observed during the experiments of Hong and Marone (2005), showing that, in a fault gouge consisting of quartz/clay mixture, a down step in normal stress causes an acceleration that does not evolve into an instability. During our creep experiments with similar quartz/clay content, even at the critical stress state for reactivation, we observe acceleration that remains slow during an increase in P_f, and we interpret this behavior as a result of the interplay between the weakening induced by fluid pressure and the intrinsic velocity strengthening behavior of clays. Our interpretation is supported by previous injection creep experiments performed on calcite fault gouge, which is characterized by a slightly velocity strengthening/neutral behavior, and a fast across fault fluid diffusion due the high permeability, ~10^{-17} m², of the fault gouge (Scuderi et al., 2017). In these experiments in correspondence of the critical stress state for reactivation the fault gouge undergoes accelerated slip (i.e., tertiary creep) that evolve in a dynamic instability, reaching peak slip velocities of >3 mm/s. These data together with those presented here strengthen our hypothesis that the combination of fault gouge frictional and hydrologic properties, and fault zone structure are key elements to evaluate the fault slip behavior induced by fluid pressurization.

4.3. Implications for Natural Fault Zones Within Shale Lithologies

Understanding the physical mechanisms that lead a fault to slip seismically or aseismically is of strategic importance to mitigate the seismic risk during underground fluid injection. With our creep experiments, instead of imposing a constant displacement rate and measure the resulting frictional response, we fix a constant shear stress and we monitor fault slip behavior while increasing fluid pressure. This type of experiments provide complementary insights for the mechanics of induced seismicity along ancient faults, where the tectonic shear stress is nearly constant and at critical values (Walsh & Zoback, 2016), and fault slip is mainly promoted by the increase of fluid pressure. In particular, our careful measurements of fault slip behavior during fluid pressure stimulations can fully capture the evolution from creep to accelerated slow slip. In addition, by keeping a constant shear stress on the fault we do not allow stress to drop during accelerated creep, nevertheless the fault slip does not evolve into a dynamic instability. Our experiments show that, at the critical stress state for fault reactivation, the mechanism for fault failure is slow but accelerated shear slip similar to that inferred for LPLD events. The evidences that there is an energy deficit during hydraulic fracturing suggest that aseismic slip or slow-slip, in the form of LPLD may play an important role in accommodating deformation (Das & Zoback, 2013; Eaton et al., 2013; Hu et al., 2017; Kumar et al., 2017).

Large-scale field experiments, where fluids were injected along natural clay-rich fault zones, have also shown that the main fault slips by aseismic creep that triggers microseismicity at the highest fluid pressure (De Barros et al., 2016; Guglielmi, Elsworth, et al., 2015). These results show that slow aseismic slip events (with a duration of ~215 s) can be triggered by fluid injection, highlighting the importance of fluid diffusion processes, within and off fault, in controlling the slip behavior (Guglielmi, Elsworth, et al., 2015). Overall, we believe that our experiments are in good agreement with in situ observations, showing that fault slip behavior during fluid injection is similar even at different scales. The coupling of these observations strengthens the hypothesis that for shale-bearing fault zones the failure mechanism is characterized by slow acceleration induced by fluid pressure. This implies that during injection operation within shale formations the monitoring of microseismicity cannot be used to fully capture the entire movement of faults. As shown by our data and in situ experiments (e.g., Elsworth et al., 2016; Guglielmi, Elsworth, et al., 2015), shale-rich faults can fail by accelerated creep and transfer stress, either mechanically or poroelastically, to adjacent fault patches that might be prone to generate a seismic instability, and trigger earthquakes (Elsworth et al., 2016).

Our mechanical model coupled with the analysis of the critical stress state for reactivation can put the basis to evaluate injection pressure that should not be overcome to avoid the risk of generating a large slow-slip event that may trigger seismicity on nearby faults that are prone to develop a frictional instability. In this context, the continuous monitoring of fault slip during injection through geodetic techniques and seismic velocity changes can reveal fundamental to evaluate fault slip evolution.

5. Conclusion

We have tested the conditions for fault reactivation induced by fluid pressurization of a shale-bearing fault gouge by developing creep experiments and compared the resulting evolution of slip behavior with the prediction retrieved from RSF analysis. We find that accelerated fault creep can be induced by an increase of fluid pressure even if the fault shows velocity strengthening behavior, which indeed should favor stable aseismic

creep. Fault movement begins well before the critical stress state for reactivation and it is modulated by fluid pressure steps suggesting that diffusion of the fluids plays a fundamental role in modulating slip behavior. At the critical stress state for reactivation the failure mechanism is characterized by slow acceleration that persists for large displacement and duration and does not evolve into a dynamic slip instability. We interpret our observation in the light of a micromechanical model that combines the evolution of fault zone structure with hydrologic and frictional properties of the fault gouge. Our model posits that in response to a fluid pressure increase, slip along overpressurized principal slip zones causes fault zone acceleration, then diffusion of the fluids coupled with the rate strengthening properties of clays favor fault to slip at a new steady state velocity that remains slow. Our data shed light on the physical mechanisms responsible for slow shear slip along shale-bearing fault gouge with important implications for natural and induced seismicity.

References

Aharonov, E., & Scholz, C. H. (2018). A physics-based rock friction constitutive law: Steady state friction. *Journal of Geophysical Research: Solid Earth*, *123*, 1591–1614. https://doi.org/10.1002/2016JB013829

Anthony, J. L., & Marone, C. (2005). Influence of particle characteristics on granular friction. *Journal of Geophysical Research*, *110*, B08409. https://doi.org/10.1029/2004JB003399

Baud, P., & Meredith, P. G. (1997). Damage accumulation during triaxial creep of Darley Dale sandstone from pore volumometry and acoustic emission. *International Journal of Rock Mechanics and Mining Science and Geomechanics Abstracts*, *34*(3-4), 24.e1–24.e10. https://doi.org/10.1016/S1365-1609(97)00060-9

Bhattacharya, P., Rubin, A. M., & Beeler, N. M. (2017). Does fault strengthening in laboratory rock friction experiments really depend primarily upon time and not slip? *Journal of Geophysical Research: Solid Earth*, *122*, 6389–6430. https://doi.org/10.1002/2017JB013936

Blanpied, M. L., Marone, C., Lockner, D. A., Byerlee, J. D., & King, D. P. (1998). Quantitative measure of the variation in fault rheology due to fluid-rock interaction. *Journal of Geophysical Research*, *103*(B5), 9691–9712. https://doi.org/10.1029/98JB00162

Boroumand, N., & Eaton, D. W. (2012). Comparing energy calculations—Hydraulic fracturing and microseismic monitoring: 74th Conference and Exhibition, EAGE, Extended Abstracts, C042. https://doi.org/10.3997/2214-4609.20148187

Brantut, N., Heap, M. J., Meredith, P. G., & Baud, P. (2013). Time-dependent cracking and brittle creep in crustal rocks: A review. *Journal of Structural Geology*, *52*, 17–43. https://doi.org/10.1016/j.jsg.2013.03.007

Brown, K. M., Kopf, A., Underwood, M. B., & Weinberger, J. L. (2003). Compositional and fluid pressure controls on the state of stress on the Nankai subduction thrust: A weak plate boundary. *Earth and Planetary Science Letters*, *214*(3-4), 589–603. https://doi.org/10.1016/S0012-821X(03)00388-1

Caffagni, E., Eaton, D. W., Jones, J. P., & van der Baan, M. (2016). Detection and analysis of microseismic events using a matched filtering algorithm (MFA). *Geophysical Journal International*, *206*, 644–658. https://doi.org/10.1093/gji/ggw168

Collettini, C., Di Stefano, G., Carpenter, B. M., Scarlato, P., Tesei, T., Mollo, S., et al. (2014). A novel and versatile apparatus for brittle rock deformation. *International Journal of Rock Mechanics and Mining Sciences*, *66*, 114–123. https://doi.org/10.1016/j.ijrmms.2013.12.005

Crawford, B. R., Faulkner, D. R., & Rutter, E. H. (2008). Strength, porosity, and permeability development during hydrostatic and shear loading of synthetic quartz-clay fault gouge. *Journal of Geophysical Research*, *113*, B03207. https://doi.org/10.1029/2006JB004634

Das, I., & Zoback, M. D. (2013). Long-period, long-duration seismic events during hydraulic fracture stimulation of a shale gas reservoir. *Geophysics*, *30*(7), 778–786. https://doi.org/10.1190/1.3609093

Davies, R., Foulger, G., Bindley, A., & Styles, P. (2013). Induced seismicity and hydraulic fracturing for the recovery of hydrocarbons. *Marine and Petroleum Geology*, *45*, 171–185. https://doi.org/10.1016/j.marpetgeo.2013.03.016

De Barros, L., Daniel, G., Guglielmi, Y., Rivet, D., Caron, H., Payre, X., et al. (2016). Fault structure, stress, or pressure control of the seismicity in shale? Insights from a controlled experiment of fluid-induced fault reactivation. *Journal of Geophysical Research: Solid Earth*, *121*, 4506–4522. https://doi.org/10.1002/2015JB012633

Den Hartog, S. A. M., Niemeijer, A. R., & Spiers, C. J. (2012). New constraints on megathrust slip stability under subduction zone P-T conditions. *Earth and Planetary Science Letters*, *353-354*, 240–252. https://doi.org/10.1016/j.epsl.2012.08.022

Den Hartog, S. A. M., & Spiers, C. J. (2014). A microphysical model for fault gouge friction applied to subduction megathrusts. *Journal of Geophysical Research: Solid Earth*, *119*, 1510–1529. https://doi.org/10.1002/2013JB010580

Dieterich, J. H. (1979). Modeling of rock friction 1. Experimental results and constitutive equations. *Journal of Geophysical Research*, *84*(B5), 2161–2168. https://doi.org/10.1029/JB084iB05p02161

Dieterich, J. H., & Linker, M. F. (1992). Fault stability under condition of variable normal stress. *Geophysical Research Letters*, *19*(16), 1691–1694. https://doi.org/10.1029/92GL01821

Domenico, P. A., & Mifflin, M. D. (1965). Water from low-permeability sediments and land subsidence. *Water Resources Research*, *1*(4), 563–576. https://doi.org/10.1029/WR001i004p00563

Eaton, D., Van der Baan, M., Tary, J., & Birkelo, B. (2013). Broadband microseismic observations from a Montney hydraulic fracture treatment, northeastern BC, Canada. *CSEG Recorder*, *38*, 44–53.

Ellsworth, W. L. (2013). Injection-induced earthquakes. *Science*, *341*(6142), 1225942. https://doi.org/10.1126/science.1225942

Elsworth, D., Spiers, C. J., & Niemeijer, A. R. (2016). Understanding induced seismicity. *Science*, *354*(6318), 1380–1381. https://doi.org/10.1126/science.aal2584

Fang, Y., Elsworth, D., Wang, C., Ishibashi, T., & Fitts, J. P. (2017). Frictional stability-permeability relationships for fractures in shales. *Journal of Geophysical Research: Solid Earth*, *122*, 1760–1776. https://doi.org/10.1002/2016JB013435

Faulkner, D. R., & Rutter, E. H. (2001). Can the maintenance of overpressured fluids in large strike-slip fault zones explain their apparent weakness? *Geology*, *29*(6), 503. https://doi.org/10.1130/0091-7613(2001)029<0503:CTMOOF>2.0.CO;2

Faulkner, D. R., Sanchez-Roa, C., Boulton, C., & den Hartog, S. A. M. (2018). Pore fluid pressure development in compacting fault gouge in theory, experiments, and nature. *Journal of Geophysical Research: Solid Earth*, *123*, 226–241. https://doi.org/10.1002/2017JB015130

French, M. E., Zhu, W., Banker, J., & Al, F. E. T. (2016). Fault slip controlled by stress path and fluid pressurization rate. *Geophysical Research Letters*, *43*, 4330–4339. https://doi.org/10.1002/2016GL068893

Goodfellow, S. D., Nasseri, M. H. B., Maxwell, S. C., & Young, R. P. (2015). Hydraulic fracture energy budget: Insights from the laboratory. *Geophysical Research Letters*, *42*, 3179–3187. https://doi.org/10.1002/2015GL063093.1

Gu, J., Rice, J., Ruina, A., & Tse, S. (1984). Slip motion and stability of a single degree of freedom elastic system with rate and state dependent friction. *Journal of the Mechanics and Physics of Solids*, *32*(3), 167–196. https://doi.org/10.1016/0022-5096(84)90007-3

Guglielmi, Y., Cappa, F., Avouac, J.-P., Henry, P., & Elsworth, D. (2015). Seismicity triggered by fluid injection—Induced aseismic slip. *Science*, *348*(6240), 1224–1226. https://doi.org/10.1126/science.aab0476

Guglielmi, Y., Elsworth, D., Cappa, F., Henry, P., Gout, C., Dick, P., & Durand, J. (2015). In situ observations on the coupling between hydraulic diffusivity and displacements during fault reactivation in shales. *Journal of Geophysical Research: Solid Earth*, *120*, 7729–7748. https://doi.org/10.1002/2015JB012158

Haines, S. H., Kaproth, B. M., Marone, C., Saffer, D. M., & van der Pluijm, B. (2013). Shear zones in clay-rich fault gouge: A laboratory study of fabric development and evolution. *Journal of Structural Geology*, *51*, 206–225. https://doi.org/10.1016/j.jsg.2013.01.002

Heap, M. J., Baud, P., Meredith, P. G., Bell, A. F., & Main, I. G. (2009). Time-dependent brittle creep in Darley Dale sandstone. *Journal of Geophysical Research*, *114*, B07203. https://doi.org/10.1029/2008JB006212

Hong, T., & Marone, C. (2005). Effects of normal stress perturbations on the frictional properties of simulated faults. *Geochemistry, Geophysics, Geosystems*, *6*, Q03012. https://doi.org/10.1029/2004GC000821

Hu, H., Li, A., & Zavala-Torres, R. (2017). Long-period long-duration seismic events during hydraulic fracturing: Implications for tensile fracture development. *Geophysical Research Letters*, *44*, 4814–4819. https://doi.org/10.1002/2017GL073582

Hubbert, M., & Rubey, W. (1959). Role of fluid pressure in mechanics of overthrust faulting. *Bulletin of the Geological Society of America*, *70*, 115–166.

Ikari, M., Saffer, D. M., & Marone, C. (2009). Frictional and hydrologic properties of clay-rich fault gouge. *Journal of Geophysical Research*, *114*, B05409. https://doi.org/10.1029/2008JB006089

Ikari, M. J., Carpenter, B. M., & Marone, C. (2016). A microphysical interpretation of rate- and state-dependent friction for fault gouge. *Geochemistry, Geophysics, Geosystems*, *17*, 1660–1677. https://doi.org/10.1002/2016GC006286

Kaneko, Y., Nielsen, S., & Carpenter, B. M. (2016). The onset of laboratory earthquakes explained by nucleating rupture on a rate-and-state fault. *Journal of Geophysical Research: Solid Earth*, *121*, 6071–6091. https://doi.org/10.1002/2016JB013143

Kawano, S., Katayama, I., & Okazaki, K. (2011). Permeability anisotropy of serpentinite and fluid pathways in a subduction zone. *Geology*, *39*(10), 939–942. https://doi.org/10.1130/G32173.1

Keranen, K., Weingarten, M., & Abers, G. (2014). Sharp increase in central Oklahoma seismicity since 2008 induced by massive wastewater injection. *Science*, *345*(6195), 448–451. https://doi.org/10.1126/science.1255802

Keranen, K. M., & Weingarten, M. (2018). Induced seismicity. *Annual Review of Earth and Planetary Sciences*, *46*, 149–174. https://doi.org/10.1146/annurev-earth-082517-010054

Kilgore, B., Lozos, J., Beeler, N. M., & Oglesby, D. (2012). Laboratory observations of fault strength in response to changes in normal stress. *Journal of Applied Mechanics*, *79*(3), 031007. https://doi.org/10.1115/1.4005883

Kohli, A. H., & Zoback, M. D. (2013). Frictional properties of shale reservoir rocks. *Journal of Geophysical Research: Solid Earth*, *118*, 5109–5125. https://doi.org/10.1002/jgrb.50346

Kumar, A., Zorn, E., Hammack, R., & Harbert, W. (2017). Long-period, long-duration seismicity observed during hydraulic fracturing of the Marcellus Shale in Greene County, Pennsylvania. *The Leading Edge*, *36*(7), 580–587. https://doi.org/10.1190/tle36070580.1

Leeman, J. R., Saffer, D. M., Scuderi, M. M., & Marone, C. (2016). Laboratory observations of slow earthquakes and the spectrum of tectonic fault slip modes. *Nature Communications*, *7*, 11104. https://doi.org/10.1038/ncomms11104

Linker, M. F., & Dieterich, J. H. (1992). Effects of variable normal stress on rock friction: Observations and constitutive equations. *Journal of Geophysical Research*, *97*(B4), 4923–4940. https://doi.org/10.1029/92JB00017

Logan, J. M., Friedman, M., Higgs, M., Dengo, C., & Shimamoto, T. (1979). Experimental studies of simulated gouge and their application to studies of natural fault zones. In *Proceedings of the VIII Conference, Analysis of Actual Fault Zones, Bedrock* (pp. 305–343). Menlo Park, CA: U.S. Geol. Survey.

Marone, C. (1998). Laboratory-derived friction laws and their application to seismic faulting. *Annual Review of Earth and Planetary Sciences*, *26*(1), 643–696. https://doi.org/10.1146/annurev.earth.26.1.643

McGarr, A., & Barbour, A. J. (2018). Injection-induced moment release can also be aseismic. *Geophysical Research Letters*, *45*, 5344–5351. https://doi.org/10.1029/2018GL078422

Moore, P. L., & Iverson, N. R. (2002). Slow episodic shear of granular materials regulated by dilatant strengthening. *Geology*, *30*(9), 843–846.

Morrow, C. A., Moore, D. E., & Lockner, D. A. (2017). Frictional strength of wet and dry montmorillonite. *Journal of Geophysical Research: Solid Earth*, *122*, 3392–3409. https://doi.org/10.1002/2016JB013658

Niemeijer, a. R., & Spiers, C. J. (2007). A microphysical model for strong velocity weakening in phyllosilicate-bearing fault gouges. *Journal of Geophysical Research*, *112*, B10405. https://doi.org/10.1029/2007JB005008

Orellana, L. F., Scuderi, M. M., Collettini, C., & Violay, M. (2018). Frictional properties of Opalinus Clay: Implications for nuclear waste storage. *Journal of Geophysical Research: Solid Earth*, *123*, 157–175. https://doi.org/10.1002/2017JB014931

Raleigh, C. B., Healy, J. H., & Bredehoeft, J. D. (1976). An experiment in earthquake control at Rangely, Colorado. *Science*, *191*(4233), 1230–1237. https://doi.org/10.1126/science.191.4233.1230

Rathbun, A. P., Marone, C., Alley, R. B., & Anandakrishnan, S. (2008). Laboratory study of the frictional rheology of sheared till. *Journal of Geophysical Research*, *113*, F02020. https://doi.org/10.1029/2007JF000815

Reinen, L., & Weeks, J. D. (1993). Determination of rock friction constitutive parameters using an iterative least squares inversion method. *Journal of Geophysical Research*, *98*(B9), 15,937–15,995. https://doi.org/10.1029/93JB00780

Ruina, A. (1983). Slip instability and state variable friction laws. *Journal of Geophysical Research*, *88*(B12), 10,359–10,370. https://doi.org/10.1029/JB088iB12p10359

Rutter, E., & Hackston, A. (2017). On the effective stress law for rock-on-rock frictional sliding, and fault slip triggered by means of fluid injection. *Philosophical Transactions of the Royal Society A*, *375*, 20160001. https://doi.org/10.1098/rsta.2016.0001

Saffer, D. M., & Marone, C. (2003). Comparison of smectite- and illite-rich gouge frictional properties: Application to the updip limit of the seismogenic zone along subduction megathrusts. *Earth and Planetary Science Letters*, *215*(1-2), 219–235. https://doi.org/10.1016/S0012-821X(03)00424-2

Samuelson, J., Elsworth, D., & Marone, C. (2009). Shear-induced dilatancy of fluid-saturated faults: Experiment and theory. *Journal of Geophysical Research*, *114*, B12404. https://doi.org/10.1029/2008JB006273

Samuelson, J., & Spiers, C. J. (2012). Fault friction and slip stability not affected by Co2 storage: Evidence from short-term laboratory experiments on North Sea reservoir sandstones and caprocks. *International Journal of Greenhouse Gas Control*, *11*(SUPPL), S78–S90. https://doi.org/10.1016/j.ijggc.2012.09.018

Sawai, M., Niemeijer, A. R., Plümper, O., Hirose, T., & Spiers, C. J. (2016). Nucleation of frictional instability caused by fluid pressurization in subducted blueschist. *Geophysical Research Letters*, *43*, 2543–2551. https://doi.org/10.1002/2015GL067569

Scholz, C. (1998). Earthquakes and friction laws. *Nature*, *391*(6662), 37–42. https://doi.org/10.1038/34097

Scholz, C. H. (2002). *The mechanics of earthquakes and faulting* (2nd ed., p. 496). New York: Cambidge University Press.

Scott, D., Marone, C., & Sammis, C. G. (1994). The apparent friction of granular fault gouge in sheared layers. *Journal of Geophysical Research*, *99*(B4), 7231–7246. https://doi.org/10.1029/93JB03361/full

Scuderi, M. M., & Collettini, C. (2016). The role of fluid pressure in induced vs. triggered seismicity: Insights from rock deformation experiments on carbonates. *Scientific Reports*, *6*(1), 24852. https://doi.org/10.1038/srep24852

Scuderi, M. M., Collettini, C., & Marone, C. (2017). Frictional stability and earthquake triggering during fluid pressure stimulation of an experimental fault. *Earth and Planetary Science Letters*, *477*, 84–96. https://doi.org/10.1016/j.epsl.2017.08.009

Segall, P., & Rice, J. (1995). Dilatancy, compaction and slip instability of a fluid-infiltrated fault. *Journal of Geophysical Research*, *100*(B11), 22,155–22,171. https://doi.org/10.1029/95JB02403

Shapiro, S. A., Rothert, E., Rath, V., & Rindschwentner, J. (2002). Characterization of fluid transport properties of reservoirs using induced microseismicity. *Geophysics*, *67*(1), 212–220. https://doi.org/10.1190/1.1451597

Tembe, S., Lockner, D. A., & Wong, T.-F. (2010). Effect of clay content and mineralogy on frictional sliding behavior of simulated gouges: Binary and ternary mixtures of quartz, illite, and montmorillonite. *Journal of Geophysical Research*, *115*, B03416. https://doi.org/10.1029/2009JB006383

Tesei, T., Lacroix, B., & Collettini, C. (2015). Fault strength in thin-skinned tectonic wedges across the smectiteillite transition: Constraints from friction experiments and critical tapers. *Geology*, *43*(10), 923–926. https://doi.org/10.1130/G36978.1

Walsh, F. R., & Zoback, M. D. (2016). Probabilistic assessment of potential fault slip related to injection induced earthquakes: Application to north-central Oklahoma, USA. *Geology*, *44*(12), 991–994. https://doi.org/10.1130/G38275.1

Warpinski, N. R., Du, J., Zimmer, U., & Service, PAH (2012). Measurements of hydraulic-fracture-induced seismicity in gas shales. *SPE Hydraulic Fracturing Technology Conference*, *27*, 6–8. https://doi.org/10.2118/151597-PA

Wibberley, C. A. J., & Shimamoto, T. (2003). Internal structure and permeability of major strike-slip fault zones: The median tectonic line in Mie Prefecture, Southwest Japan. *Journal of Structural Geology*, *25*(1), 59–78. https://doi.org/10.1016/S0191-8141(02)00014-7

Wojatschke, J., Scuderi, M. M., Warr, L. N., Carpenter, B. M., & Saffer, D. M. (2016). Experimental constraints on the relationship between clay abundance, clay fabric and frictional behavior for the Central Deforming Zone of the San Andreas Fault. *Geochemistry, Geophysics, Geosystems*, *17*, 3865–3881. https://doi.org/10.1002/2016GC006500

Yeck, W. L., Hayes, G. P., McNamara, D. E., Rubinstein, J. L., Barnhart, W. D., Earle, P. S., & Benz, H. M. (2017). Oklahoma experiences largest earthquake during ongoing regional wastewater injection hazard mitigation efforts. *Geophysical Research Letters*, *44*, 711–717. https://doi.org/10.1002/2016GL071685

Zecevic, M., Daniel, G., & Jurick, D. (2016). On the nature of long-period long-duration seismic events detected during hydraulic fracturing. *Geophysics*, *81*(3), KS113–KS121. https://doi.org/10.1190/geo2015-0524.1